A landslide runout model for sediment transport, landscape evolution and hazard assessment applications

Jeffrey Keck[1,2], Erkan Istanbulluoglu[1], Benjamin Campforts[3], Gregory Tucker[4,5], Alexander Horner-Devine[1]

[1] University of Washington, Civil and Environmental Engineering, Seattle, WA, USA
[2] Washington Department of Natural Resources, Forest Resources Division, Olympia, WA, USA
[3] Department of Earth Sciences, Vrije University, Amsterdam, Netherlands
[4] Department of Geological Sciences, University of Colorado Boulder, Boulder, CO, USA
[5] Cooperative Institute for Research in Environmental Sciences (CIRES), University of Colorado Boulder, Boulder, CO, USA

Correspondence to: Jeffrey Keck (keckje@gmail.com)

Abstract

We developed a new rule-based, cellular-automaton algorithm for predicting the hazard extent, sediment transport and topographic change associated with the runout of a landslide. This algorithm, which we call MassWastingRunout (MWR), is coded in Python and implemented as a component for the package Landlab. MWR combines the functionality of simple runout algorithms used in landscape evolution and watershed sediment yield models with the predictive detail typical of runout models used for landslide inundation hazard mapping. An initial Digital Elevation Model (DEM), a regolith depth map, and the location polygon of the landslide source area are the only inputs required to run MWR to model the entire runout process. Runout relies on the principle of mass conservation and a set of topographic rules and empirical formulas that govern erosion and deposition. For the purpose of facilitating rapid calibration to a site, MWR includes a calibration utility that uses an adaptive Bayesian Markov Chain Monte Carlo algorithm to automatically calibrate the model to match observed runout extent, deposition and erosion. Additionally, the calibration utility produces empirical probability density functions of each calibration parameter that can be used to inform probabilistic implementation of MWR. Here we use a series of synthetic terrains to demonstrate basic model response to topographic convergence and slope, test calibrated model performance relative to several observed landslides, and briefly demonstrate how MWR can be used to develop a probabilistic runout hazard map. A calibrated runout model may allow for region-specific and more insightful predictions of landslide impact on landscape morphology and watershed-scale sediment dynamics, and should be further investigated in future modelling studies.

1. Introduction

Over geologic timescales, landslides and their runout shape the topographic expression of mountain ranges and channel networks (e.g., Campforts et al., 2022; Korup, 2006; Larsen and Montgomery, 2012; Montgomery and Dietrich, 1988). Over more pragmatic engineering and environmental risk management timescales, landslides and their runout can inundate and destroy infrastructure (e.g., Kean et al., 2019) but also support numerous ecosystem

benefits, including carbon and nutrient transport from hillslopes to channels and the creation of riparian habitat (Benda et al., 2003; Bigelow et al., 2007; Goode et al., 2012). Therefore, explicit representation of landslide runout is a necessary component of: (1) landslide inundation hazard assessments, with emphasis on inundation extent and flow depth (e.g., Frank et al., 2015; Han et al., 2015); (2) watershed sediment yield models, with emphasis on the mobilization, deposition and type of sediment carried by the landslide (e.g., Bathurst and Burton, 1998; Istanbulluoglu,et al., 2005); and (3) landscape evolution models, with emphasis on topographic change prediction (e.g., Tucker and Bras, 1998; Istanbulluoglu and Bras, 2005; Campforts et al., 2022).

Landslide runout processes can be generalized into three phases: initiation, erosion, and deposition. After a landslide initiates, it may break apart and flow as a relatively dry debris slide, or it may mix with surface runoff to become a debris flow. The mobility of the mass wasting material and resulting erosion/deposition pattern often varies as a function of runout topography and initial relief and size of the landslide (Iverson, 1997). Mobility may also be impacted by substrate liquefaction (Hungr and Evans, 2004) and landslide basal cataclasis (Shaller et al., 2020). As the runout material moves downslope, flow depth varies as a function of channel width (Kean et al., 2019), which in turn impacts erosion rates (Schürch et al., 2011). Theoretical, field and laboratory observations indicate that erosion rates may also depend on the moisture content of the channel bed (Iverson, 2012; McCoy et al., 2012), flow grainsize (Egashira et al., 2001) and granular stress within the flow (Capart et al., 2015). The slope at which deposition begins is controlled by the grain-to-water ratio and friction angle of the runout material (Takahashi, 2014; Major and Iverson, 1999; Zhou et al., 2019) but the friction angle of the runout material may vary as a function of the grains in the flow and fluidization (Hutter et al., 1996). Lateral levees often form along the edges of the flow (Major, 1997; Whipple and Dunne, 1992; Shaller et al., 2020) and deposition at the distal end of the flow may occur as layered accretion (Major, 1997) or as the emplacement of a single, massive deposit (Shaller et al., 2020). If the water content of the runout material is high enough, as the solid fraction of the distal end of the flow compresses, the water is squeezed out and may continue as an immature debris flow (sensu Takahashi, 2014) or intense bedload (sensu Capart & Fraccarolo, 2011), extending the runout distance (e.g., Shaller et al., 2020).

Landslide inundation hazard models aim to accurately predict the runout extent and/or flow depths of a runout event and may include some or most of the above processes in the model. Example models include: (1) site-specific-empirical/statistical models that use simple geometric rules and an estimate of the total mobilized volume (initial landslide body + eroded volume) or a growth factor (e.g., Reid et al., 2016); (2) detailed, continuum-based mechanistic models, which conceptualize the runout process as a single-phase or multiphase flow using the depth-integrated Navier-Stokes equations for an incompressible, free-surface flow (i.e., shallow water equations; Frank et al., 2015; Han et al., 2015; Iverson and Denlinger, 2001; Medina et al., 2008) and often (though not always) require pre-knowledge of the total mobilized volume (e.g., Barnhart et al., 2021; Han et al., 2015); (3) reduced or appropriate complexity flow-routing models (e.g., Murray, 2007) that use rule-based abstractions of the key physical processes that control the flow (Clerici and Perego, 2000; Guthrie and Befus, 2021; Gorr et al., 2022; Han et al., 2017, 2021; Horton et al., 2013; Liu et al., 2022) and are typically implemented using just the initial landslide location and volume but often rely on heavy, site specific parameterization and; (4) hybrid modelling approaches that combine mechanistic

71 models with empirical and reduced complexity approaches (D'Ambrosio et al., 2003; Iovine et al., 2005; Lancaster et
72 al., 2003; McDougall and Hungr, 2004).

73 For landscape evolution and watershed sediment yield applications (herein collectively referred to as watershed
74 sediment models, WSMs), the runout model must be scalable in both space and time, and capable of modelling the
75 entire runout process given an internally modelled initial landslide body (e.g. Tucker and Bras, 1998; Doten et al.,
76 2006; Campforts et al., 2022). As such, computationally efficient and parsimonious reduced complexity runout models
77 that evolve the terrain and transfer sediment are often preferred in WSMs, however with simplifications that can
78 restrict model ability to accurately replicate observed inundation extent or depositional patters. Such simplifications
79 include omitting debris flow erosion and bulking in runout channels, limiting flow to only a single cell in the steepest
80 downstream direction, and assuming debris flows only occupy the width of a single cell (e.g., Tucker and Bras, 1998;
81 Istanbulluoglu and Bras, 2005) or link of a channel network (Benda and Dunne, 1997).

82 We developed a new, reduced complexity landslide runout model, called MassWastingRunout (MWR), that bridges
83 the scalable functionality of WSMs with the predictive accuracy of landslide inundation hazard models, without the
84 computational overhead of a detailed mechanistic representation of the runout process, or difficult parameterization
85 typical of other models. MWR models landslide runout starting from the source area of the landslide, making it easily
86 compatible with WSMs that internally determine the initial landslide body size and location. MWR tracks sediment
87 transport and topographic change downstream, and evolves the attributes of the transport material, making it suitable
88 for sediment yield studies. MWR can be calibrated by adjusting just two parameters (S_c and q_c, described in Section
89 2) and is augmented with a Bayesian Markov Chain Monte Carlo (MCMC) calibration utility that automatically
90 parameterizes model behavior to observed runout characteristics (e.g., erosion, deposition, extent). MWR also
91 includes a built-in utility called MWR Probability, designed for running an ensemble of simulations to develop
92 probabilistic landslide runout hazard maps, making MWR suitable for hazard assessment applications.

93 In this paper, we present the conceptualization and numerical implementation of the MWR model (Section 2), describe
94 the calibration utility and probabilistic implementation of MWR (Section 3) and demonstrate basic model response to
95 topographic convergence and slope on a series of synthetic terrains (Section 4). Event-scale applications to replicate
96 observed runout extent, sediment transport, and topographic change at four topographically and geologically unique
97 field sites (see Figure 1) are discussed (Section 5). We test MWR's predictive ability using the parameterization of
98 one site to predict runout hazard at a nearby site and show a brief example of Monte Carlo model runs to determine
99 runout probability from initial landslide source areas defined by an expert-determined potentially unstable slope or a
100 hydrologically-driven landslide hazard model (Section 6). We conclude with a short summary of MWR model
101 performance and suggest how a calibrated MWR can be incorporated into WSMs.

102

Figure 1. Example landslides used to evaluate calibrated MWR performance: (a) Cascade Mountains, WA: a large debris avalanche over steep, broadly convergent terrain (photo credit: Stephen Slaughter). (b) Black Hills, WA: large debris flows over a broadly convergent, gently sloped valley (photo credit: Stephen Slaughter). (c) Rocky Mountains, CO: a moderate sized debris avalanche over a steep, unconfined to divergent hillslope. (d) Olympic Mountains, WA: small debris flows in steep, highly convergent channels. Image scale varies with depth, but approximate scale is indicated at the location of the scale bar.

2. Description of the MassWastingRunout model

2.1 Overview of the cellular-automaton modelling approach

MWR is coded as a discrete cellular automaton (CA) model. CA models apply a set of equations or rules (deterministic or probabilistic) to individual cells of a grid to change the numerical or categorical value of a cell state (e.g., Codd, 1968). In earth sciences, CA models are widely used to model everything from vegetation dynamics (e.g., Nudurupati et al., 2023) to lava flows (e.g., Barca et al., 1993) to geomorphic transport, in which gravitationally directed erosion

114 and depositional processes modify a digital elevation model (DEM) representation of a landscape (e.g., Chase, 1992;

115 Crave & Davy, 2001; Murray & Paola, 1994; Tucker et al., 2018). Existing CA-based landslide runout models include

116 models by Guthrie and Befus (2021), D'Ambrosio et al. (2003) and Han et al. (2021). In all of these models, runout

117 behavior is controlled by topographic slope and rules for erosion and deposition but conceptualization and

118 implementation differ.

119 In MWR, mass continuity is central to model conceptualization. Of the wide range of landslide runout processes

120 described in the introduction, MWR explicitly represents erosion, deposition, and flow resistance as a function of the

121 initial landslide body and downslope terrain. Material exchange between the runout material and underlying regolith

122 as well as flow resistance determines runout extent and landscape evolution. Model rules are designed such that they

123 can be parameterized from field measurements. Finally, in MWR, most computations occur only at the location of

124 moving debris, in a manner analogous to the "mobile" cellular automaton implementation of Chase (1992).

125 Chase (1992) modelled precipitation-driven surface erosion by randomly placing single packets of precipitation on a

126 DEM, which then moved from higher elevation to lower elevation grid cells, eroding and transporting sediment as a

127 function of the slope between the cells. The individual packets of precipitation were referred to as precipitons. In

128 MWR, since we route the downslope progression of debris from a specified mass wasting source area, we refer to

129 these packets of debris as "debritons". The debritons represent debris flux, here defined as a volume of debris

130 transferred per model iteration per grid-cell area, $[m^3/m^2/iteration]$ and are equivalent to the flow depth in the cell.

131 The present implementation of the MWR algorithm is coded in Python and developed as a component of the Landlab

132 earth surface modeling toolkit (Barnhart et al., 2020; Hobley et al., 2017). MWR uses the Landlab raster model grid,

133 which consists of a lattice of equally sized, rectangular cells. Topographic elevation, derived topographic properties

134 like slope and curvature, and other spatially varying attributes such as regolith depth and grain size, are recorded at

135 nodes in the center of each cell (see Figure 5 of Hobley et al., 2017). In the subsequent sections we describe the model

136 theory. All parameters and variables used in the theory are listed in the Notation section.

137 **2.2   Mobilization of the initial mass wasting source material (Algorithm 1):**

138 To initiate MWR, the user provides maps of initial topography, regolith depth, and the location and depth of the mass

139 wasting source material (e.g., the initial landslide body). Each raster model grid node in the mass wasting source

140 material is designated as a debriton (Figure 2, iteration $t = 0$) with a magnitude equal to the mass wasting source

141 material depth at the node and basal elevation equal to the initial topography minus the mass wasting source material

142 depth at the node. The basal elevation can be thought to represent the rupture or slip surface of the source material and

143 the redistribution (flux) of each debriton to its downslope nodes (receiver nodes) is determined as a function of the

144 slope of the slip surface. At the lowest-elevation debriton of the source material, flux to its downslope nodes is

145 determined using the surface slope of the initial DEM (see flow direction of lowest node in Figure 3a). This

146 implementation helps to ensure that the lowest-elevation debriton in the mass wasting source material moves

147 downslope and movement of upslope debritons are impacted by the geometry of the mass wasting source material.

148 For example, the receiver nodes of the lowest-elevation debriton in the initial landslide body illustrated in Figure 2

149 (node 45) would be identified as those among the eight neighboring nodes whose initial topographic elevation is less

150 than the initial topographic elevation of node 45 while for the debriton at node 51, the receiver nodes would be
151 identified as those among the eight neighboring nodes whose topographic elevation is less than the basal elevation of
152 the debriton (see Figure 3a).

153
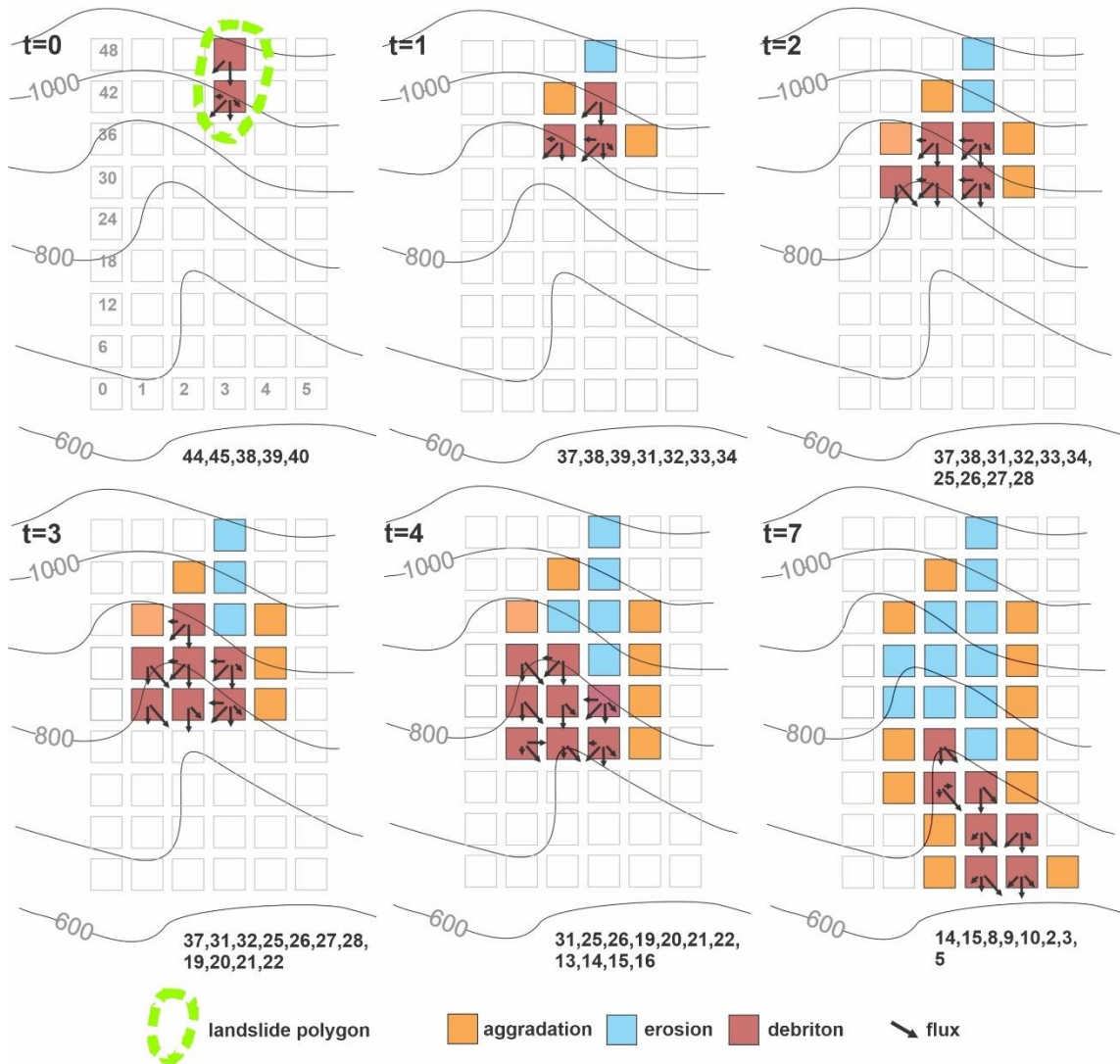
Figure 2. Illustration of the mobilization and runout of an initial mass wasting source area (landslide body) down a steep,
convergent slope. Variable t indicates model iteration (not time). Notice how the flow elongates and widens as the model progresses
and the number of receiver nodes (numbers listed at bottom of each panel) and quantity of mobilized material increase.

157
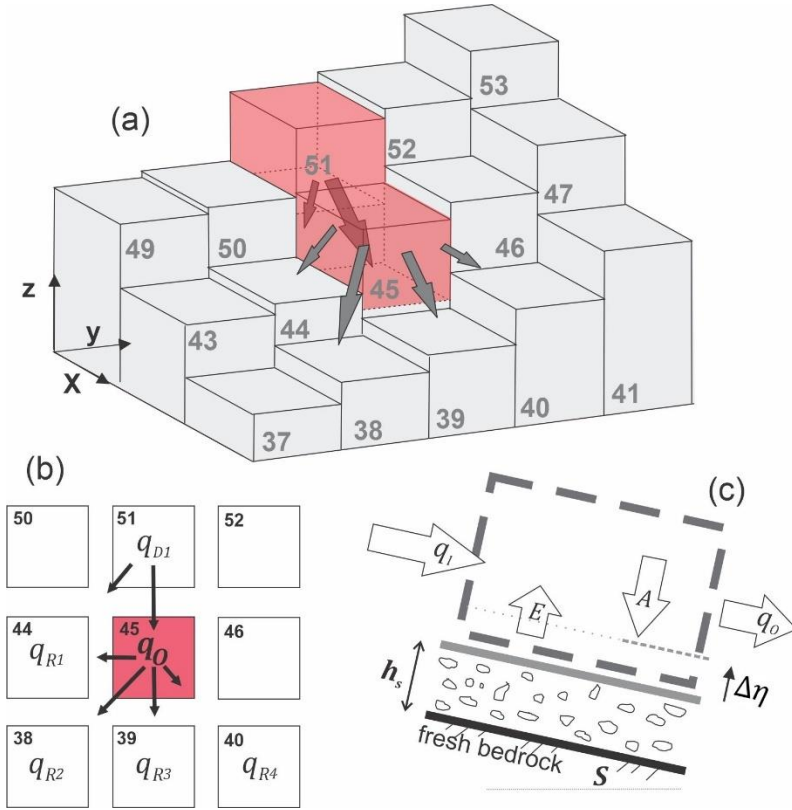
Figure 3. (a) Three-dimensional illustration of iteration $t = 0$ in Figure 2, showing initial source material nodes (represented by red cells) and flux towards downslope nodes. (b) Distribution of q_O to downslope nodes 38, 39, 40 and 44; (c) illustration of mass continuity applied to any node that receives a debriton.

2.3 Flow routing and rules for erosion, deposition and resistance (Algorithm 2)

Algorithm 2 is essentially the runout model. It determines how each debriton traverses and modifies the landscape. After receiver nodes from the first model iteration are determined in Algorithm 1 (iteration t=0), Algorithm 2 is repeatedly implemented until all material has deposited (i.e., there are no debritons). Each debriton moves one grid cell per model iteration, the larger the landslide size, the more iterations necessary to evacuate the landslide slip surface. As each debriton moves, it may erode or aggrade the landscape, impacting the movement of any upslope debritons. As is common with other reduced complexity models (e.g., Guthrie and Befus, 2021), we assume that inertial effects have negligible impact on flow behavior (i.e., the kinematic flow approximation) and the downslope redistribution of a debriton or flux to each of a node's i-th receiver nodes (q_{R_i}) is determined as a function of topographic slope (slope of terrain under the debriton). We do this using the Freeman (1991) multiple flow direction algorithm:

$$q_{R_i} = q_O \frac{S_i^a}{\sum_{i=1}^{Nr} S_i^a} \tag{1}$$

where q_O is the total out-going flux from the node and has units of depth [m] per model iteration, Nr is the number of receiving nodes, i is the index for each receiver node (e.g., $i = 1, 2 \dots Nr$) and S_i is the underlying topographic slope to the i-th receiver node (Figure 3b). The Freeman (1991) multiple flow direction algorithm is a commonly used

176 approximation for two-dimensional flow, and in this implementation it is handled by a pre-existing Landlab flow-

177 routing component. The exponent a controls how material is distributed to downslope nodes, with higher values

178 causing narrower flow (Holmgren 1994). In a braided river cellular-automaton model, Murray and Paola (1997) used

179 an approximation for turbulent shallow water flow to justify $a = 0.5$ (which is the exponent on the slope factor in

180 channel friction laws). For our application, we found MWR provided a closer fit to observed mass wasting runout if

181 $a = 1$, suggesting that the material behavior is more similar to linear-viscous shear flow than to wall-bounded turbulent

182 shear flow (e.g., as the runout debris flows downslope, it tends to spread less than shallow, turbulent water). The total

183 incoming flux (again, in units [m] per model iteration) towards a given node (q_I), is determined by summing the flux

184 from each of the node's donor nodes:

185 $q_I = \sum_{j=1}^{Nd} q_{D_j}$ (2)

186 Where Nd is the number of donor nodes, and q_{D_j} is the flux from node D_j (the j-th donor node, $j = 1,2… Nd$; Figure

187 3b).

188 As noted by Tucker and Hancock (2010), the flow depths calculated from two-dimensional flow approximations like

189 (1) can be influenced by the choice of grid-size used to represent the terrain. Additionally, as simplified multi-

190 directional flow models like (1) neglect the pressure and momentum forces in the movement of flow, they can result

191 in inaccurate flow width and depth estimates, depending on terrain slope and convergence. Rengers et al. (2016) noted

192 these limitations when using a kinematic wave approximation of the shallow water equations, as this approximation

193 lacks a pressure term that facilitates the spreading of the modelled water surface. While the topographic controls on

194 mass conservation are adequately represented by (1), our model bears such limitations when calculating flow depth

195 and width. Moreover, in our model, flow depth is used to determine a depth-dependent erosion rate. As such, in order

196 to avoid unrealistically high flow depths (and erosion rates), we constrain flow depth to an upper limit as:

197 $h = min (h_{max}, q_I)$ (3)

198 Where h_{max} is an effective upper limit to flow depth, that in practice can be approximated as the maximum observed

199 flow depth, as inferred from field indicators or assigned based on expert judgement (See Section 5) and h is the

200 corrected flow depth used to calculate flow shear stress. This correction allows erosion rates to vary with flux but

201 prevents unreasonably large values. This flow depth correction does not violate the conservation of mass and runout

202 mass balance, as h is only used to calculate flow shear stress.

203 To determine aggradation (A) at a node, we use a critical slope (S_c) constraint that permits computationally-rapid

204 distribution of q_I over multiple nodes. Critical slope constraints or rules are common to many reduced complexity and

205 landscape evolution models. Chen et al. (2023) showed that when flow inertia can be ignored, S_c can be approximated

206 from the surface slope of observed deposits. Several landscape evolution models use a S_c-based nonlinear, nonlocal

207 aggradation scheme (e.g., Campforts et al., 2020; Carretier et al., 2016) but when this rule is implemented with the

208 debriton framework described above, unreasonably tall deposits result when q_I is large and slope at the node (S) $<<$

209 S_c. To resolve this problem, aggradation depth can be limited to $A \leq S_c \Delta x$, (where Δx grid cell length), but we found

210 that this constraint results in long deposits that parallel the underlying slope when q_I is large. Instead, MWR computes

211   the aggradation depth at a node assuming that the aggradation will spread over N_a nodes until all of q_I is deposited

212   and that the surface slope of the overall deposit will be equal to S_c, as shown in Figure 4 and described as follows.
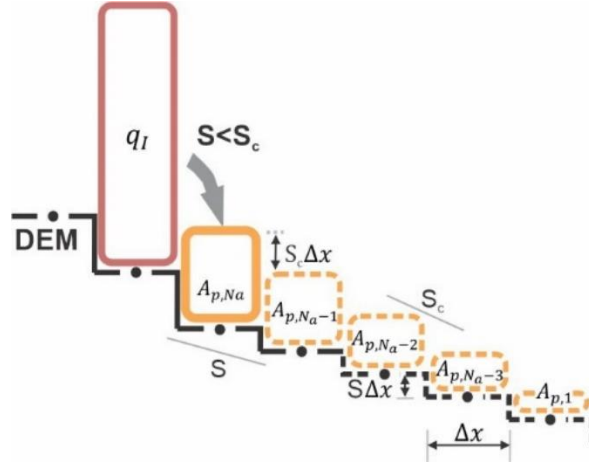
213

214   **Figure 4.** Illustration of aggradation rule used in MWR when q_I is assumed to spread over 5 nodes ($N_a = 5$). Solid yellow box
215   indicates aggradation amount at a given node. Dashed yellow boxes and lines indicate the geometry of assumed the aggradation
216   beyond the node. Dots along DEM surface are nodes.

217   Aggradation at a node is determined as:

218     $$A = \begin{cases} 0 & , & S \geq S_c \\ min(A_{p,N_a}, q_I) & , & S < S_c \end{cases} \tag{4}$$

219   Where S is the steepest slope to the node's eight neighbouring nodes, A_{p,N_a} is a potential aggradation depth necessary

220   to form the beginning of the overall deposit that: (1) begins at the node and spreads over N_a consecutive nodes; (2)

221   has a total volume equal to $q_I \Delta x^2$; (3) a surface slope equal the critical slope S_c and; (4) an underlying topographic

222   slope equal to S and assumed constant over the N_a consecutive nodes of deposition. From these assumptions, we can

223   analytically define A_{p,N_a} and N_a as a function of q_I, S_c and S as follows:

224   First, q_I, calculated from (2), can be used to calculate $A_{p,i}$ by expressing q_I as the sum of the N_a deposits that make

225   up the overall deposit as:

226     $$q_I = \sum_{i=1}^{N_a} A_{p,i} \tag{5}$$

227   where $A_{p,i}$ is the i-th deposition amount in the overall deposit and $i = 1$ is the last node of deposition ($A_{p,1}$; see Figure

228   4). Since we assume the deposit slope and underlying topographic slope are uniform, the deposition amount at any of

229   the N_a nodes can be determined from $A_{p,1}$ as:

230     $$A_{p,i} = A_{p,1} + (i-1)\Delta x (S_c - S) \tag{6}$$

231   From (6) we can re-write (5) as a function of $A_{p,1}$ and rearrange to define $A_{p,1}$ as a function of q_I:

232     $$A_{p,1} = \frac{1}{N_a} q_I - \frac{N_a - 1}{2} \Delta x (S_c - S) \tag{7}$$

233   Substituting (7) into (6) and solving for $i = N_a$, we get an expression for A_{p,N_a}:

234 $$A_{p,N_a} = \frac{1}{N_a}q_I + \frac{N_a-1}{2}\Delta x(S_c - S)$$ (8)

235 Equation (8) can be rearranged into a quadratic equation and solved for N_a as:

236 $$N_a = \frac{-A_{p,1}+\frac{1}{2}\Delta x(S_c-S)\pm\sqrt{\left(A_{p,1}-\frac{1}{2}\Delta x(S_c-S)\right)^2+2\Delta x(S_c-S)q_I}}{\Delta x(S_c-S)}$$ (9)

237 We use (8) to solve for A_{p,N_a} and (9) to solve for N_a assuming $A_{p,1} = 1/2\,\Delta x S_c$ and rounding the positive solution to

238 the nearest integer. When implemented using a single debriton, released on a two-dimensional hillslope as illustrated

239 in Figure 4, the debriton deposits over N_a nodes at a uniform slope equal to S_c. When implemented on an actual three-

240 dimensional terrain, the interaction between multiple debritons in multiple directions creates a complex deposit whose

241 slope changes with S_c.

242 To determine erosion depth (E) [m/iteration], we constrain E to the lesser of a potential erosion depth, h_e, and local

243 regolith depth, h_r:

244 $$E = min\,(h_r, h_e)$$ (10)

245 where h_e is computed as a function of the basal shear stress of the flow, τ [Pa], (Equations 12 and 13) and the critical

246 shear stress (τ_c) of the regolith at the node [Pa]:

247 $$h_e = k(\tau - \tau_c)^f$$ (11)

248 The coefficient k is an erodibility parameter [m/Pa^f]. Stock and Dietrich (2006) showed that k encapsulates substrate

249 properties. If h_e is used to represent erosion over geomorphic time scales, with repeated debris flow occurrences in a

250 single model iteration, k becomes associated with debris flow length and frequency (Perron, 2017). In our application

251 since we are modelling the erosion associated with a single runout event, as represented by the downslope movement

252 of the debritons, the coefficient k therefore needs to scale h_e on the order of the average erosion depth caused by a

253 single debriton. Using this logic, k can be computed using the observed average erosion depth and an estimated length

254 of the runout material that caused the erosion. Further details on how we determine k from observed runout are

255 included in the Appendix. The exponent f controls the non-linearity of h_e with shear stress. Many authors (e.g., Chen

256 & Zhang, 2015; Frank et al., 2015; Shen et al., 2020) use a value of 1 for f but field measurements by Schürch et al.

257 (2011) (see their Figure 3) suggest that f may be less than 1 if τ is assumed to vary linearly with flow depth,

258 particularly at flow depths greater than 3 meters.

259 MWR includes two options for defining τ: (1) a quasi-static basal shear stress approximation or (2) a grain-size-based

260 shear stress approximation. The quasi-static basal shear stress approximation (e.g., Takahashi, 2014) is defined as:

261 $$\tau = \rho g h \sin\theta$$ (12)

262 where ρ is the density of mass wasting material (grain and water mixture) [kg/m^3], g is gravity [m/s^2], h is the adjusted

263 flow depth described in (3) and θ is the topographic slope ($\tan^{-1}(S)$) measured in degrees.

264 The grain-size-based shear stress approximation is defined using an empirical formula by Bagnold (1954):

265 $$\tau = \sigma \tan\varphi$$ (13)

266   Where σ is normal stress [Pa], φ is the collision angle between grains, measured from the vertical axis (See Bagnold,

267   1954), with a value of $\tan \varphi$ typically equal to 0.32. Stock and Dietrich (2006) defined σ as:

268    $\sigma = \cos \theta v_s \rho_s D_s{}^2 \left(\frac{du}{dz}\right)^2$ (14)

269   Where v_s is the volumetric solids concentration, ρ_s is density of the solids [kg/m³], u is flow velocity [m/s], z is depth

270   below the flow surface [m], du/dz is the shear strain rate [1/s] and D_s is the representative grain size [m]. Stock and

271   Dietrich (2006) suggested that D_s corresponds to a small percentile of the coarsest fraction of the runout material (D_{88}

272   to D_{96}) and they approximated du/dz as:

273    $\frac{du}{dz} = \frac{u}{h}$ (15)

274   Solely for the purpose of computing du/dz, we approximate velocity at a node using a grain-size dependent empirical

275   formula for debris flow velocity by Julien and Paris (2010) as:

276    $u = 5.75 u^* log \left(\frac{h}{D_s}\right)$ (16)

277   Where u^* is shear velocity $\left(\sqrt{gh \tan \theta}\right)$. Substituting (16), (15), (14) and (13) into (11) yields a grain-size dependent

278   approximation for h_e that mimics the non-linear erosion response to flow depth in Schürch et al. (2011). Additionally,

279   this form of τ is advantageous because it permits landslide-driven erosion rates to scale with landslide grain size,

280   which can vary by lithologic region (e.g., Roda-Boluda et al., 2018). As will be shown in Section 5, we obtained

281   reasonable model calibration at multiple sites by defining D_s from the coarser grain sizes observed in the field at

282   existing runout-deposits, road-cuts and tree-throw pits.

283   Once A [m] and E [m] have been determined, total out-going flux per iteration, q_O [m] is determined as (see Figure

284   3c):

285    $q_O = \begin{cases} q_I - A + E, & q_I \geq q_c \\ 0 & , & q_I < q_c \end{cases}$ (17)

286   Where q_c is a threshold flux for deposition. When $q_I < q_c$, q_I deposits and q_O becomes zero. The threshold flux q_c

287   conceptually represents the flow depth below which flow resistance is large enough to cease the forward momentum

288   of the flow, whether in the form of internal friction or friction due to vegetation and obstructions (e.g., large clasts or

289   logs). The density and water content of q_I, A, and E are treated as uniform and surface runoff, such as channelized

290   stream flow or hillslope-infiltration-excess runoff, that might mix with q_I A, or E is ignored. Once q_I, A, q_O and E

291   have been determined, change in elevation at a node ($\Delta \eta$) is calculated as:

292    $\Delta \eta = A - E$ (18)

293   Attributes (e.g., grain size, organic content or any other attribute that is transferred in the flow) of the debriton and

294   regolith are updated using a volumetric-weighted average approach. First, for each regolith attribute being tracked by

295   the model, the attribute value delivered to a node from its donor nodes (ξ_D) is determined as:

296    $\xi_D = \frac{\xi_D \cdot q_D}{q_I}$ (19)

297   where $\boldsymbol{q_D}$ is a vector containing all q_{D_j} sent to the node, $\boldsymbol{\xi_D}$ is a vector containing the incoming attribute values for

298   each q_{D_j}, and q_I is the sum of incoming flux from donor nodes defined by (2).

299   Second, the attribute value sent from a node to its receiver nodes (ξ_R) is determined as:

300     $\xi_R = \frac{\xi_{t-1}E + \xi_D(q_I - A)}{q_O}$ (20)

301   where ξ_{t-1} is the attribute value at the node before any aggradation (i.e., the previous iteration attribute value). Finally,

302   the attribute value at the node, updated to account for erosion and aggradation (ξ) is:

303     $\xi = \frac{\xi_{t-1}(h_r - E) + \xi_D A}{A + h_r - E}$ (21)

304   Regolith thickness (h_r) and topographic elevation (η) are updated at a node as:

305     $\eta = \eta_{t-1} + \Delta\eta$ (22)

306     $h_r = h_{r\,t-1} + \Delta\eta$ (23)

307   Where η_{t-1} and $h_{r\,t-1}$ are the topographic surface elevation and regolith thickness at the node from the previous

308   model iteration. After regolith thickness and topographic elevation have been updated for each debriton, the multi-

309   direction slope of the DEM, which is needed for implementing Equation (1) the next model iteration, is recomputed.

310   As the DEM is updated following each model iteration, topographic pits or flat topography may form. These features

311   have no slope or slope inwards and obstruct debriton movement. To allow a debriton to pass an obstruction, we rely

312   on a simple work-around: upon encountering the obstruction, the debriton is directed to itself and some portion of the

313   debris is deposited based on (4). At the end of the model iteration, the node elevation and slope are updated. During

314   the next iteration, if the remaining mobile debris is no longer obstructed, it moves to its downslope node(s). If the

315   node is still obstructed, it is again sent to itself until either all material has deposited or the elevation of the node

316   exceeds that of its neighbour nodes, allowing the debriton to move downslope.

317   **3.**   **Calibration and MWR probability**

318   **3.1**   **Calibration utility**

319   MWR includes a calibration utility that uses an adaptive, Bayesian Markov Chain Monte Carlo (MCMC) algorithm

320   described by Coz et al. (2014) and Renard et al. (2006). The calibration utility determines: (1) a single set of parameters

321   that best match MWR output to an observed landslide runout dataset and (2) posterior parameter probability

322   distribution functions (PDF). The observed runout dataset can consist of a single or multiple landslides. Depending

323   on user input, MWR simultaneously or sequentially models runout from each landslide source area in one model run.

324   To use the calibration utility, the user provides an initial (prior) guess of the parameter values and their respective

325   PDFs that calibrate the MWR to a specific site. Then, the calibration utility randomly selects a set of trial parameter

326   values (Λ) from the prior PDFs and runs MWR using Λ. Once the model has completed the run, the algorithm evaluates

327   the posterior likelihood of the parameter set ($L(\Lambda)$) as the product of model ability to replicate observed runout

328   (described below) and the prior likelihood of the parameter set. After the first $L(\Lambda)$ has been determined, the utility

329   selects a new set of parameters (Λ_{t+1}) by jumping some distance (described below) from each parameter in Λ space.

330   Depending on the value of $L(\Lambda_{t+1})$, the algorithm either stays at Λ or moves to Λ_{t+1}. This Markov process is repeated

331   a user-specified number of times. Jump direction is random, but the algorithm is adaptive because the jump distance

332   changes depending on if $L(\Lambda_{t+1}) > L(\Lambda)$ occurs more than a user specified threshold value. For a detailed description

333   of the algorithm see Coz et al. (2014).

334   The $L(\Lambda)$ index is estimated as the product of the prior probability of the selected parameter values, $p(\Lambda)$, and three

335   other performance metrics as:

336     $L(\Lambda) = p(\Lambda) * \Omega_T * \frac{1}{\Delta\eta_E{}^2} * \frac{1}{Q_{s_E}{}^2}$ (24)

337   where Ω_T is the Lee-Salle index (Heiser et al., 2017) for evaluating model planimetric fit and $\Delta\eta_E$ and Q_{s_E} are new

338   dimensionless indices, proposed for this study (described below). The index $\Delta\eta_E$ is the volumetric error of the

339   modelled topographic change over the entire model domain normalized by the observed total mobilized volume (initial

340   landslide body + erosion volume). The index Q_{s_E} is the mean-cumulative sediment transport error along the modelled

341   runout path normalized by the observed mean cumulative flow. Larger values of Ω_T and smaller values of $\Delta\eta_E$ and

342   Q_{s_E} indicate modelled runout more closely fits observed. Note that we add a value of 1 to Ω_T and use the squared-

343   reciprocal values of $\Delta\eta_E$ and Q_{s_E} in (24) so that the magnitude of $L(\Lambda)$ is always equal to or greater than zero and

344   increases with improved fit. The metric Ω_T is written as:

345     $\Omega_T = \frac{\alpha-\beta-\gamma}{\alpha+\beta+\gamma} + 1$ (25)

346   where α, β and γ are the areas of matching, overestimated and underestimated runout extent, respectively.

347   The index $\Delta\eta_E$ is determined as:

348     $\Delta\eta_E = \sqrt{\frac{\sum_{i=0}^{p}[(\Delta\eta_{Oi} - \Delta\eta_{Mi})\Delta x^2]^2}{V^2}}$.   (26)

349   Where V is observed total mobilized volume and p is the number of nodes in the area made up of the matching,

350   overestimated and underestimated areas of modelled runout extent and $\Delta\eta_{Mi}$ and $\Delta\eta_{Oi}$ are the modelled and observed

351   topographic change [m] at the i-th node within that extent.

352   To calculate Q_{s_E}, we first determine the cumulative sediment transport volume (Q_s) at each node, j along the runout

353   profile, in a manner similar to the flow volume/mass balance curves in Fannin and Wise (2001) and Hungr and Evans

354   (2004):

355     $Q_s = -\Delta x^2 \sum_{i=1}^{u_j} \Delta\eta_{i,j}$ (28)

356   where $\Delta\eta_{ij}$ is the topographic change [m] at the i-th node located above the elevation of node j, and u_j is the total

357   number of nodes located above node j. Q_s is computed for both the observed and modelled runout (Q_{sO} and Q_{sM}

358   respectively) and Q_{s_E} is determined as:

359 $$Q_{s_E} = \sqrt{\frac{\frac{1}{r}\Sigma_{j=1}^{r}(Q_{sO}-Q_{sM})^2}{\overline{Q_{sO}}^2}}$$ (29)

360 Where r is the number of nodes along the runout profile, and $\overline{Q_{sO}}$ is the observed mean cumulative flow.

361 As will be detailed in Section 5, field estimates for S_c and q_c vary over the length of the runout path. To account for

362 the heterogeneity of S_c and q_c, we estimate prior PDFs of potential S_c and q_c values from field/remote sensing

363 measurements. Then, from model calibration to a DEM-of-Difference (pre-runout DEM subtracted from the post-

364 runout DEM; DoD) using the calibration utility, we produce posterior PDFs of S_c and q_c and find a single S_c and q_c

365 pair that allows the modelled DoD to best replicate the observed DoD (i.e., the S_c and q_c pair with the highest $L(\Lambda)$

366 value).

367 We run the calibration utility using a single Markov chain of 2000 repetitions. At most sites, the model converged

368 relatively quickly on a solution and we therefore didn't account for burn-in or evaluate convergence (e.g., Gelman et

369 al., 2021) and considered 2000 repetitions adequate. Future implementations of the calibration utility may include

370 multiple chains, burn-in and a check for convergence. As a final note, many debris flow runout models are evaluated

371 using Ω_T or variations of Ω_T alone (e.g., Gorr et al., 2022; Han et al., 2017) and the MWR calibration utility can also

372 be run solely as a function of Ω_T (i.e., runout extent). However, we found that calibration based on Ω_T alone results

373 in high parameter equifinality (e.g., Beven 2006); multiple parameter sets result in an equally calibrated model as

374 evaluated by Ω_T. As such, we recommend calibrating debris flow/landslide runout models to an observed DoD. If

375 repeated lidar is available, a DoD can be obtained from before and after scans of the observed runout event.

376 Alternatively, a DoD can be created by hiking the observed runout event and mapping field-interpreted erosion and

377 deposition depths. Additional details on how we prepared DoDs for multiple sites are included in the Supplementary

378 Material.

379

3.2   Mapping landslide runout hazard

381 MWR includes an additional utility called MWR Probability that produces landslide runout probability maps. MWR

382 Probability repeatedly runs MWR a user specified Np times, each repetition with a different, randomly sampled

383 parameter set from the posterior parameter PDFs produced by the calibration utility. MWR Probability includes three

384 options for specifying the initial mass wasting source material: (1) a user-provided landslide source area polygon(s)

385 based on field and/or remote sensing observations; (2) a user-defined hillslope that is susceptible to landslides (e.g.,

386 potentially unstable slope), where landslide area and location are randomly selected within, but no larger than the

387 hillslope; this option is useful when the extent of a potential landslide is unknown; and (3) a series of mapped landslide

388 source areas within a watershed, as determined by an externally run Monte Carlo landslide initiation model (e.g.,

389 Hammond et al., 1992; Strauch et al., 2018) ; this option is useful for regional runout hazard applications. If using

390 Option 1, modelled runout probability represents uncertainty in MWR parameterization. If using Option 2 or 3,

391 modelled runout probability reflects uncertainty in both MWR parameterization and landslide location and size.

392   For all three run options, each model iteration begins with the same initial topography. After Np model simulations,

393   Np different versions of the post-runout landscape are created and, probability of runout at each node is determined

394   as:

395    $$P(\Delta\eta) = \frac{num(|\Delta\eta|>0)}{Np}$$ (30)

396   where $num(|\Delta\eta| > 0)$ is the number of times topographic elevation at a node changes as a result of erosion or

397   deposition from the Np model runs. Probability of erosion or aggradation can be determined by replacing the

398   numerator in (30) with $num(\Delta\eta < 0)$ or $num(\Delta\eta > 0)$ respectively.

399   **4.   Basic model behavior**

400   We evaluate basic model behavior using a series of virtual experiments. The virtual experiments consist of six

401   synthetic terrains including: (A) a planar slope that intersects a gently sloped plane (S = 0.001); (B) a planer slope

402   with a constriction, that intersects a gently-sloped plane; (C) a planar slope that has a bench mid-slope and then

403   intersects a gently-sloped plane; (D) a concave up, uniform-convergence slope; (E) a concave up, variable-

404   convergence slope that widens (convergence decreases) in the downslope direction; (F) a convex up, variable-

405   convergence slope that widens (convergence decreases) in the downslope direction. On each terrain, a 30-meter wide,

406   50-meter long and 3-meter deep landslide is released from the top of the terrain. All six terrains are covered by a 1-

407   meter thick regolith and use the same parameter values (S_c = 0.03, q_c = 0.2 m, k = 0.01, D_s = 0.2 m). Each terrain is

408   represented using a 10-m grid. Experiment results are shown in Figure 5.
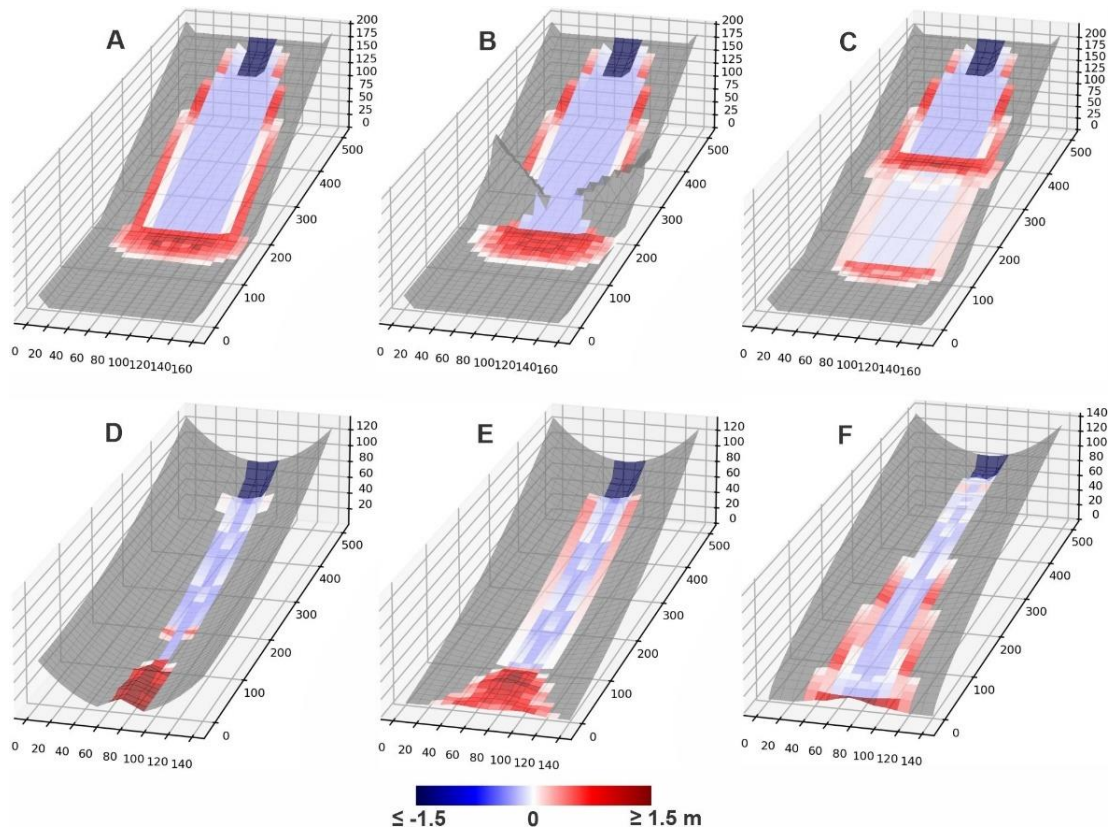
409

410 **Figure 5.** Shaded, 3-D visualizations of model response to six different synthetic terrains, colored according to the DoD of the
411 final runout surface. Shading is to scale. Red indicates a positive change in the elevation of the terrain (aggradation) and blue
412 indicates a negative change (erosion). The 3-D visualization of the DoD is exaggerated by a factor of 5 to make visible in figure.
413 Grid size is 10 meters.

414   On Terrain A, the landslide spread as it moved downslope and formed levees along the edge of the runout path. The

415   width of the spread was a function of the multiple flow direction algorithm and resistance along lateral margins of the

416   runout as represented by q_c. At the slope break at the base of the slope, the material deposited at an angle controlled

417   by S_c. On Terrain B, the flow initially eroded and deposited identical to Terrain A but near the slope break, the

418   topographic constriction forced flow depth to increase and exceed q_c, minimizing the formation of levees (because

419    $q_o > q_c$) and resulted in a slightly larger deposit at the base of the slope. On Terrain C, landslide runout was again

420   initially identical to the runout on Terrain A; however, upon intersecting the mid-slope bench, most of the runout

421   material deposited. A small, thinner portion did continue past the bench but eroded at a lower rate than upslope of the

422   bench. Upon intersecting the flat surface at the base of the hillslope, the runout material deposited.

423   On Terrain D, the landslide and its runout were confined to the center of the convergent terrain and only deposited

424   once the slope was less than S_c. The slide never widened because the uniformly convergent channel shape prevented

425   spreading and the narrower flow width maintained a higher flow depth, which prevented the formation of levees. On

426   Terrain E, the landslide again deposited once slope was less than S_c but because topographic convergence of Terrain

427   E decreases in the downslope direction, as the runout material moved downslope, the deposit spread more than on

428   Terrain D, which caused thinner flow and deposition along margins of the runout path. On the final terrain, Terrain F,

429   slope is always greater than S_c so deposition was limited to levees along the edge of the flow that formed as the runout

430   spread in response to decreasing convergence.

431   MWR model behavior can be summarized as follows: The displacement and deposition of landslide material predicted

432   by MWR responds to topography in a reasonable manner. Flow width increases as convergence decreases (e.g, Terrain

433   F), which in turn reduces flow depth. Lower flow depths cause lower erosion rates and reduce aggradation extent.

434   Conversely, modelled flow depth increases when convergence increases (e.g., Terrain B). Where the flow encounters

435   broadly convergent or planer slopes, lateral levee deposits form, a common feature of landslides reported in the

436   literature and at sites reported here (see Section 5) that detailed mechanistic models can struggle to reproduce (e.g.,

437   Barnhart et al., 2021).

438   We do not attempt to compare MWR modelled flow with the output of shallow-water-equation based models or

439   observed granular flows (e.g., Medina et al., 2008; McDougall and Hungr, 2004; Iverson and Denlinger, 2001; Han

440   et al., 2015). The cellular automaton representation in MWR does not model the time-dependent evolution of debris

441   flow velocity and depth, and conceptually moves debris instantaneously at each iteration, as driven by changes in the

442   evolving topographic elevation field. Because of that, only the final outcome (modelled runout extent, sediment

443   transport and topographic change) of MWR can be compared with other models or observed runout, which we do in

444   the next section. Also, as described in Section 2.3, behaviour of the multiple flow direction algorithm does vary with

445   grid size. Using a coarser or finer grid, without adjusting model parametrization, could potentially change the runout

446   patterns shown in Figure 5.

447   **5.   Model Validation**

448   **5.1   Overview**

449   In this section, we demonstrate the ability of a calibrated MWR to replicate observed runout extent, sediment transport

450   and topographic change at field sites located in the western USA and summarize model calibration results with an

451   evaluation of MWR calibration relative to terrain attributes of the observed runout paths. Note that simply calibrating

452   a model to match field data does not constitute a satisfactory test of model predictive ability (Iverson, 2003). Strategic

453   testing, which involves calibrating the model to one site or period of time and then running the calibrated model at a

454   separate site or period of time (Murray, 2013), is a better indicator. Two of our validation sites, the Cascade Mountains

455   and Olympic Mountains sites, include two separate landslides and subsequent runout and we test model predictive

456   ability at these sites in Section 6.

457   Calibrated model performance is demonstrated at the following field sites (see Figure 6a for locations and observed

458   runout extent): (1) two runout events over the same hillslope in the Cascade Mountains (Washington state [WA],

459   USA): a large debris avalanche in 2009 (Cascade Mountains, 2009) and a moderately-sized debris flow in 2022

460   (Cascade Mountains, 2022) that inundated and flowed within a first-to-second order channel until perpendicularly

461   intersecting a narrow river valley several hundred meters below the landslide (Figure 1a); (2) debris flows in the Black

462   Hills (WA) sourced from a small failure along the toe of a deep-seated landslide (Black Hills, South) and a moderately-

463 sized debris avalanche from a large road fill (Black Hills, North) that flowed several kilometers along a relatively

464 wide, broadly convergent channel before stopping (Figure 1b); (3) a single, moderately-sized debris avalanche in the

465 Rocky Mountains (Rocky Mountains), the majority of which flowed several hundred meters over a broadly convergent

466 to divergent hillslope in Colorado (Figure 1c); and (4) a 30-year chronology of small landslides and subsequent debris

467 flows in the Olympic Mountains (WA) in steep, highly convergent channels that flowed well over a kilometer and

468 coalesced into a single runout deposit in a dendritic, channelized watershed (Olympic Mountains; Figure 1d). All

469 landslides initiated during heavy rainfall or rain-plus-snowmelt storm events (WRCC, 2022; NRCS, 2022; Table 1)

470 but their runout varied in terms of erosion rate, grain size (Figure 6b), depositional behavior (Figure 6c) and the

471 topographic convergence of the underlying terrain.

472 **Table 1.** Landslide and runout characteristics

site	Cascade Mountains 09	Cascade Mountains 22	Black Hills, south	Black Hills, north	Rocky Mountains	Olympic Mountains
initial landslide body length., ℓ [m] [a]	185	55	80	75	40	45
initial landslide body width [m] [a]	86	53	13	69	25	15
initial landslide body depth [m] [a]	6.9	7.5	1.4	3.6	4.6	1.5
initial landslide body vol. [m^3] [a]	110,000	22,000	1,500	18,500	4,600	1025
2-day cumulative precipitation + snowmelt [mm]	120+85	140+75	205+50	205+50	193+0	100 - 220 + ?
maximum grain size [m]	0.316	0.316	0.48	0.206	0.984	0.8
slope range of positive-net deposition [%]	1 - 15	1 - 15	<1 - 10	<1 - 8	16 - 25	5 - 15
average flow depth in scour zone [m]	4	2	2	3	3	3
average channel slope in scour zone [m/m]	0.25	0.25	0.15	0.15	0.4	0.3
average channel width in scour zone [m]	45	20	25	35	55	10
length of erosion, [m]	600	340	1210	1345	360	2550
erosion area, A_e [m^2]	28,400	6,600	22,800	52,400	20,800	28,900
erosion volume, $\sum E \Delta x^2$ [m^3] [b]	44,547	5,125	12,332	26,815	34,275	33,725
average erosion per unit length of runout debris, $\bar{E}/\ell$, [m/m]	0.0085	0.014	0.0068	0.0068	0.041	0.026
k	0.020	0.034	0.017	0.020	0.076	0.051
growth factor, [m^3/m]	74.2	15.1	10.2	19.9	95.2	13.2
average observed $|\Delta\eta|$ [m]	2.4	2.2	0.53	0.63	0.89	1.4
total erosion volume / total mobilized volume [c]	0.29	0.19	0.89	0.59	0.88	0.97

473 [a] for the Olympic Mountains site, width and depth are average values and length and volume are defined as the
474 average cumulative value upstream of each runout path
475 [b] excludes landslide volume
476 [c] total mobilized volume = initial landslide body + erosion volume
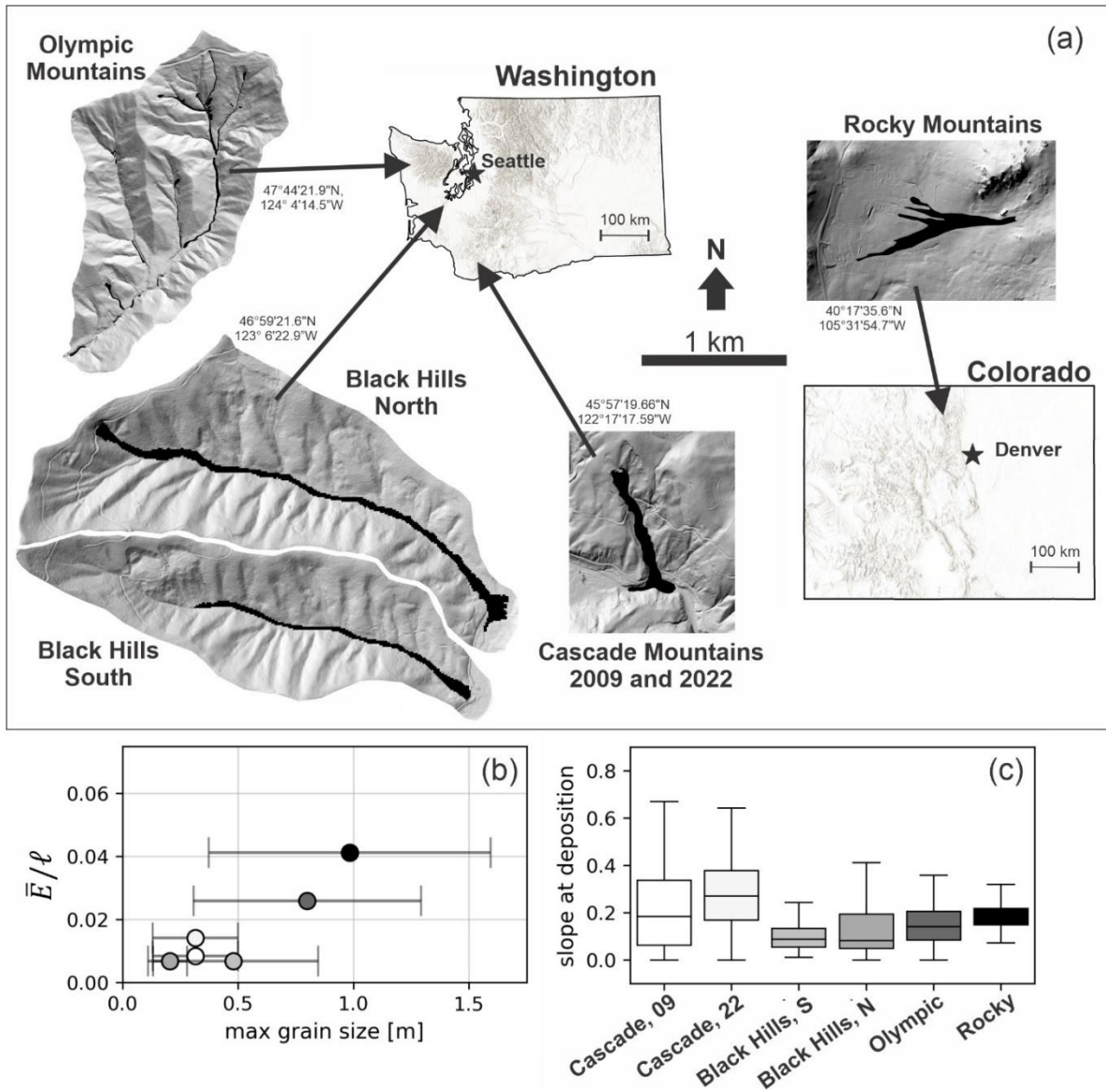
Figure 6. (a) Landslide locations in Washington and Colorado states. Coordinates next to each site are WGS84. Shaded DEMs of each site are shown at the same scale. (b) Observed average erosion rate per unit landslide length ($\bar{E}/\ell$) relative to the observed average-maximum grainsize. Error bars indicate standard deviation. (c) Underlying topographic slope of observed deposition.

5.2 Model setup and field parameterization

Each model was set up on a 10-meter grid representation of the pre-event DEM with either a uniform or spatially varying regolith thickness (detailed for each site in the Supplementary Material). The length (ℓ) and area of the initial mass wasting source material (e.g., the initial landslide body) was interpreted from a combination of Lidar DEM, air-photo and field observations. The average depth of the initial landslide body was measured in the field or from the DoD. The volume of the initial landslide body was determined as the area times the average depth. An average width was determined as the area divided by the length. At the Olympic Mountains site, where the observed runout pattern formed as a result of multiple landslides, (see Supplementary Material), landslide depth and width values listed in

489   Table 1 are average values and landslide length, area and volume values are the average cumulative value upstream

490   of each runout path. At all locations, we use Equation (13) to approximate shear stress. We field-surveyed each site,

491   noting the maximum flow depth (inferred from initial landslide body volume and height of scour marks and width of

492   channel in erosion zone), typical deposition and erosion depths and the size of the largest grains in the runout deposits.

493   We estimated parameter values from these field and remote observations (See Table 1). A site-specific value for k

494   was determined as a function of the observed average erosion depth (determined as total erosion volume divided by

495   the erosion area, $\bar{E}$) relative to the length of the runout debris, which we approximated as the length of the initial

496   landslide body(ℓ). Further details are described in the Appendix.

497   The volume of the initial landslide body ranged from 400 to 110,000 m^3 across sites. At all sites, erosion and

498   subsequent entrainment added to the total mobilized volume (initial landslide body + erosion volume), but the

499   contribution was highly variable. The erosion volume divided by the total mobilized volume was as low as 0.19 at the

500   Cascade Mountains, 2022 landslide to as high as 0.97 at the Olympic Mountains landslides (Table 1).

501   The average maximum grain size varied from 0.2 m at the Black hills sites to nearly 1 m at the Rocky Mountains Site

502   (Figure 6b, Table 1). Values of $\bar{E}/\ell$ ranged from 0.007 to 0.041 [m/m] with the highest rate occurring at the Rocky

503   Mountains landslide and the lowest at the Black Hills sites. Details on grain-size samples and data collected in the

504   field are described in the Supplementary Material. In terms of growth factors (average volumetric erosion per unit

505   length of the erosion-dominated region of the runout path, Hungr et al., 1984; Reid et al., 2016) values ranged from

506   10 m^3/m at the Black Hills South site to 95 m^3/m at the Rocky Mountains site (Table 1).

507   The median values of topographic slopes at which observed deposition occurred (i.e., $\Delta\eta > 0$, inferred from the DoD)

508   ranged between 0.1 and 0.3 across sites, while deposition was also observed in much steeper (>0.4) slopes, and much

509   flatter slopes at some sites (Figure 6c). The slope of channel reaches where net deposition (cumulative erosion and

510   deposition; e.g., Guthrie et al., 2010, inferred from field observations) was positive tended to be lowest at the Black

511   Hills site (<1% to 10%) and highest at Rocky Mountains site (16% to 25%).

512   We defined uniform prior distributions of S_c and q_c and then used the calibration utility to find the best-fit parameter

513   values (parameter values corresponding to the highest $L(\Lambda)$). Minimum and maximum values of S_c were initially

514   estimated from the range of observed slope of areas of positive-net deposition (Table 1). Minimum and maximum

515   values of q_c were set as 0.01 to 1.75, which roughly represents the range of minimum observed thickness of debris

516   flow termini in the field at all of the validation sites. For the purpose of implementing the calibration utility, we

517   prepared a DoD of each site. The DoD was determined either from repeated lidar or field observations as detailed in

518   the Supplementary Material.

519   **5.3   Calibration and model performance**

520   Markov chains, colored according to the likelihood index, $L(\Lambda)$ are plotted in the S_c - q_c domain, along with

521   histograms of sampled S_c and q_c values for each landslide in Figure 7. Each Markov chain includes 2000 model

522   iterations. The runtime for 2000 model iterations depended on model domain, landslide size and number of landslides

523   modelled but varied from roughly 1.5 hours for the Cascade Mountains, 2022 landslide to 6 hours for the Olympic

524 Mountains site on a 2016 2.1 GHz Intel Core Xeon, 32 GB memory desktop. The chains show a wide array of

525 sampling patterns and parameter ranges but broadly speaking, at all sites, the algorithm jumped within S_c- q_c space

526 towards higher $L(\Lambda)$, to form bell-shaped posterior distributions for each parameter. Depending on the landslide type,

527 the calibration algorithm converged on different S_c- q_c pairs. For example, at the Cascade Mountains site, the

528 calibration utility converged to smaller q_c and S_c values for the 2009 event (Figure 7a), which permitted thinner flows

529 over lower slopes and effectively made the 2009 modelled runout more mobile relative to the 2022 modelled runout

530 (Figure 7b). At the Rocky Mountains site (Figure 7e), a relatively high q_c value helps limit the lateral extent of the

531 modelled runout that in the observed runout was controlled by standing trees (see Supplementary Material).
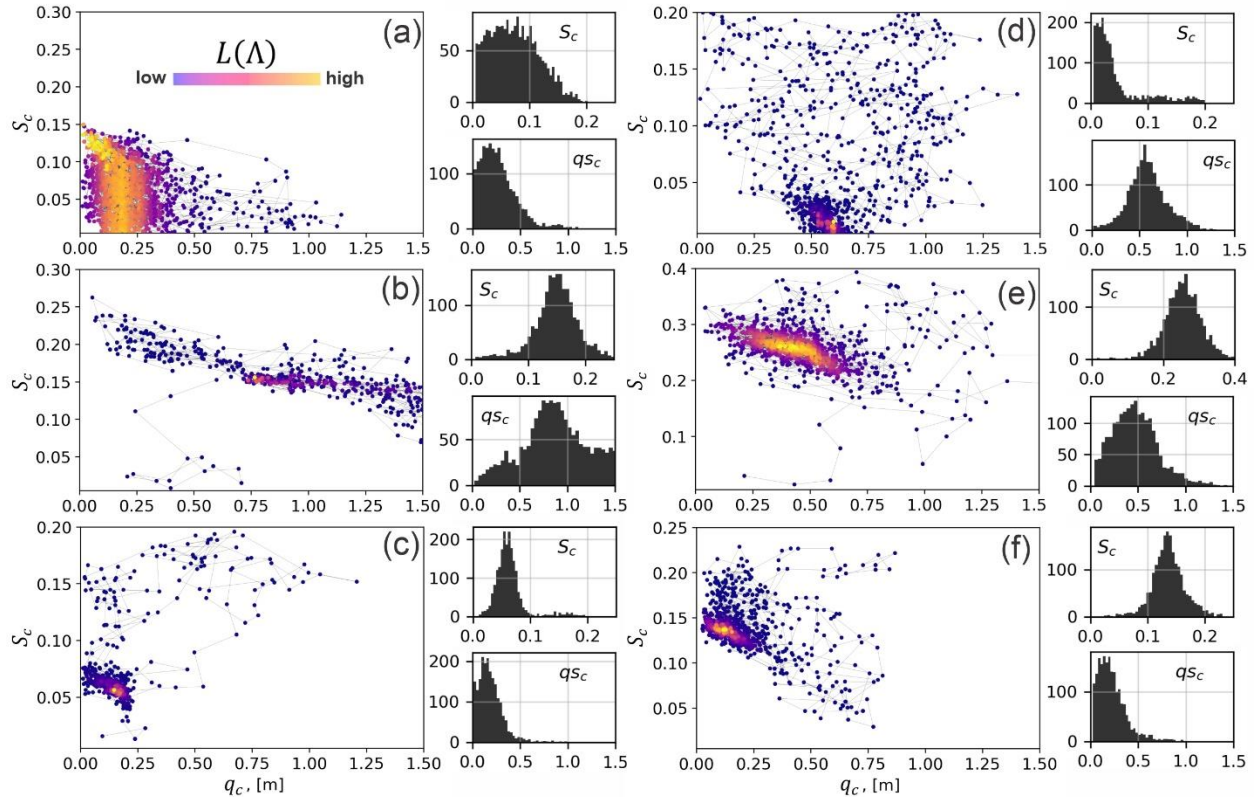
532
533 **Figure 7.** MWR calibration results for (a) Cascade Mountains, 2009; (b) Cascade Mountains, 2022, (c) Black Hills, South; (d)
534 Black Hills, North; (e) Rocky Mountains and; (f) Olympic Mountains. Each result shows a scatter plot of the sampled S_c and q_c
535 values, colored by their relative $L(\Lambda)$ value. Line between points indicates jump direction. Note y-axis scale differs between
536 plots. To the right of each scatter plot are histograms of the iterated S_c and q_c parameters, which can be normalized to represent
537 an empirical, posterior PDF of the possible S_c and q_c values that calibrate MWR to the site. Histogram y-axis is count and x-axis
538 is S_c or q_c, as indicated on the histogram.

539 Profile plots of modelled Q_s and maps of the modelled planimetric runout extent, colored to indicate where the runout

540 matched (α), overestimated (β) or underestimated (γ) the observed runout are shown in Figure 8. Values of Ω_T we

541 obtained with MWR are comparable or higher than reported values of Ω_T in the literature that used a variety of models

542 (Gorr et al., 2022; Barnhart et al., 2021; Note, to compare Ω_T values to those studies, subtract 1 from values reported

543 in this study). Across the sites, the volumetric error of the model, $\Delta\eta_E$, ranges between 6% and 15% (median 9.1%)

544 of the total mobilized volume. An overall <10% volumetric error is reasonable considering the low number of

545 parameters required to calibrate MWR and that empirical estimates of total mobilized volume used to run other runout

546   models can vary by as much of an order of magnitude (e.g., Gartner et al., 2014: Barnhart et al., 2021). Model

547   performance in predicting cumulative sediment transport along the runout profile was within similar error ranges.

548   Except for the Rocky Mountains site where MWR consistently modelled wider-than-observed flow, the mean-

549   cumulative sediment transport error along the runout profile (Q_{s_E}) was limited between 5% to 19% of the mean

550   cumulative flow determined from the observed DoD.

551   MWR generally successfully replicates observed sediment transport along the runout path via model parameterizations

552   that are unique to each landslide. For example, the profile plots of Q_s at the Cascade Mountains site (Figure 8a and

553   8b) show that during the 2009 landslide, all of the runout material flowed past the first 750 meters of the runout path.

554   During the 2022 landslide, material began to deposit just down slope of the initial landslide source area, as both

555   observed and modelled Q_s reverse slope, indicating a decrease in cumulative flow. Model comparisons in the Cascade

556   Mountains site were limited to the upper 750 m of the hillslope because a large portion of the runout material was lost

557   to fluvial erosion in the valley (see Supplementary Material).

558   MWR also successfully replicates the observed sediment transport patterns at the Olympic Mountains site (profile plot

559   of Q_s in Figure 8f) and to a lesser degree, the Rocky Mountains site (Figure 8e). This finding is notable, because at

560   the Olympic Mountains and Rocky Mountains sites, observed runout extent and sediment depositional patterns were

561   heavily impacted by woody debris or standing trees (See Supplementary Material).

562   Using a fixed grid size of 10-m might have impacted model performance in some areas like the Olympic Mountains

563   and Cascade Mountains, 2022 sites where MWR tended to over-estimate the runout width (yellow zones in Figures

564   8f and 8b). While a 10-m DEM is generally accepted as a good balance between model detail and computational

565   limitations (e.g., Horton et al., 2013), for small landslides, the 10-m grid was close to the width of the channels that

566   controlled observed runout (see Figure 1d) and may not have accurately represented the terrain. Thus, modelled flow

567   was less topographically constrained and tended to flow over a wider area than observed.

568   Also, because MWR does not have an explicit representation of flow momentum, it may show poor performance in

569   regions of the runout path where flow momentum is the primary control on runout extent. For example, at the Cascade

570   Mountains, 2009 slide, MWR underestimates a short section of slope-perpendicular flow over a bench. Review of

571   model behavior for this slide (Figure 9) shows how MWR successfully mimics diverging flow around a broad ridge

572   upslope of the bench (iteration t=28 in Figure 9), but afterwards continues to follow topographic slope and converges

573   too rapidly into a narrow ravine along the west edge of the bench (iteration t=40 in Figure 9; compare to runout scar

574   in air photo and underestimated region on topographic bench in Figure 8a).

575   Nonetheless, overall, calibration was best at the Cascade Mountains, 2009 landslide (values of Ω_T are highest and

576   values of $\Delta\eta_E$ and Q_{s_E} are lowest) and poorest at the Rocky Mountains and Olympic Mountains sites (Values of Ω_T

577   are lowest and Q_{s_E} and $\Delta\eta_E$ are highest). At both the Rocky Mountains and Olympic Mountains sites, because we

578   lacked repeat lidar, we created the DoD from a map of field estimated erosion and deposition depths and estimated

579   the pre-event DEM. The lower calibration scores may indicate that field estimated DoDs were not as accurate as those

580   determined via lidar differencing. Another source of uncertainty that we have not addressed in our study is regolith

581   thickness. At most sites, we used a uniform thickness. As regolith thickness limits maximum erosion depth (i.e.,

582   Equation 10) using a spatially accurate regolith thickness may improve model performance. Finally, except for the

583 Rocky Mountains site, where topography was unusually planar and the model seemed to consistently over-estimate

584 flow width, at most sites, MWR does not appear to have a strong systematic bias in modeled output, which suggests

585 that when applied to convergent terrain, MWR may not have any structural weaknesses. In the next section, we

586 evaluate model performance relative to runout path topography.
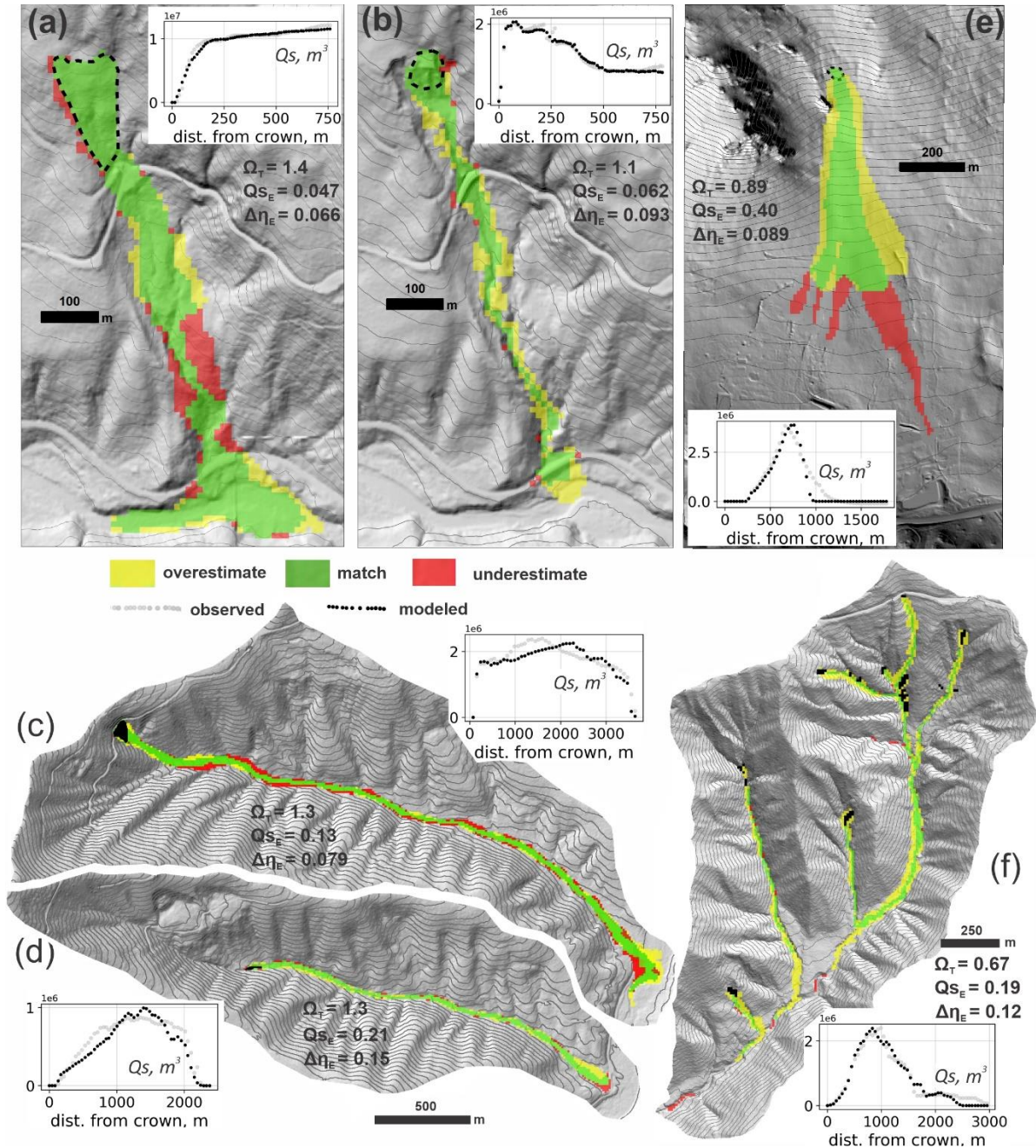
587

588 **Figure 8.** Calibrated model performance as indicated by maps of modeled runout extent, profile plots of observed and modeled

589 cumulative sediment transport along the centerline of the runout path (Q_s, see Equation 28) and reported values of Ω_T, $\Delta\eta_E$ and

590 Q_{s_E}. Y-axis label for profile plots of Q_s indicated on plot. In all maps, up is north except in (e), north is towards the left. (a)

591 Cascade Mountains, 2009; (b) Cascade Mountains, 2022; (c) Black Hills, North; (d) Black Hills, South; (e) Rocky Mountains; (f)

592 Olympic Mountains.

593
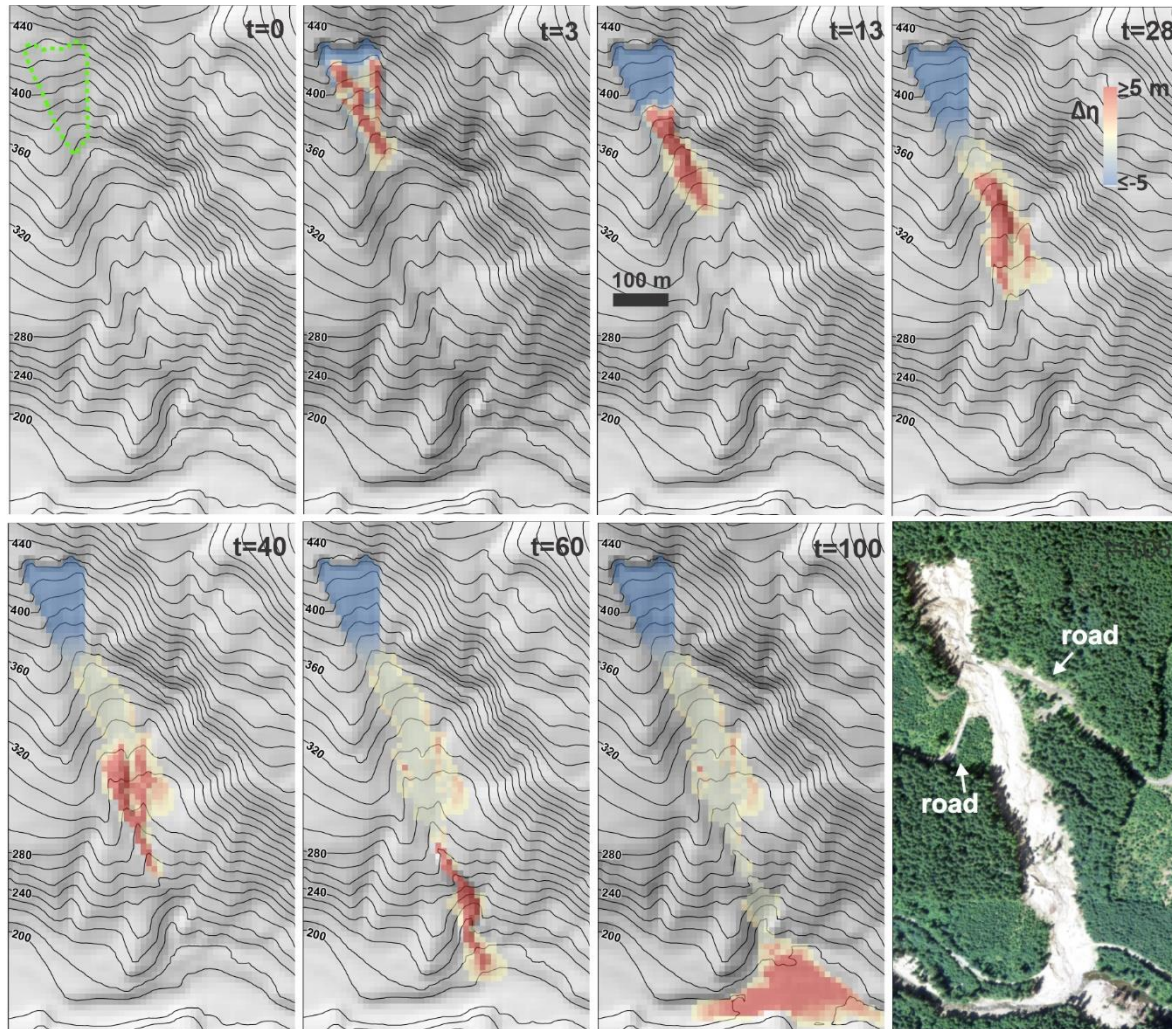
Figure 9. Illustration of modeled runout of the Cascade Mountains, 2009 landslide beginning from the initial movement of the landslide body to final deposition in the river valley that demonstrates MWR response to topography. Note how the landslide slip surface directs the initial flow. Topography lines reflect the underlying terrain, which is updated after each iteration. Air photo in last panel shows observed runout extent. Note that upper road is not part of the observed landslide runout path.

5.4 Runout path topography and model performance

Model behavior at the Rocky Mountains site suggests that MWR performance may systematically vary with topography (e.g., it may not perform as well on planar hillslopes). To check for systematic model variation, we compared model performance with three topographic indices described by Chen & Yu (2011). The indices are computed from the terrain in the observed runout extent and include the relief ratio (H/L), mean total curvature (κ) and the mean specific stream power index (SPI). The index H/L equals the average slope of the runout path (or relative relief), determined as the total topographic relief of the runout (measured from the center of the initial landslide to the end of the runout path) divided by the horizontal length of the runout and indicates the mobility of the runout. Index κ represents topographic convergence, which is the second derivative of the terrain surface, with increasingly

608   positive values of index κ reflecting growing topographic convergence and concave-up channel profile (e.g.,

609   Istanbulluoglu et al., 2008). The index SPI is determined as the natural log of the product of the contributing area and

610   slope. Indices κ and SPI are computed at each node in the runout extent and model performance is compared to the

611   mean value.

612   Comparison of model performance with respect to the topographic indices in Figure 10 shows: slightly improved

613   model performance over runout paths that are less convergent (lower SPI and κ values) and on steeper terrain (higher

614   H/L) but neither trend is significant. The latter finding appears to be mostly a result of how well modelled sediment

615   transport and topographic change (Q_{s_E} and $\Delta\eta_E$) replicated observed, as there does not appear to be a trend in Ω_T with

616   H/L and the two best performing models (both Cascade Mountains landslides) had the lowest (best) Q_{s_E} values and

617   low $\Delta\eta_E$ values. Both findings are likely impacted by the grid size we used to represent terrain. As noted above, at all

618   sites we used a 10-m grid, but at some sites 10-m doesn't quite capture the relief of channelized topography that

619   controlled observed runout, leading to modelled runout that was considerably wider than observed and causing low

620   Ω_T value (this is especially true at the Olympic Mountains site, Figure 10a, b and c). Also, it is important to note that

621   these indices were calculated for the extent of the observed debris flows and may not represent the topographic form

622   that controlled the model.

623   In summary, using the calibration utility, we showed how MWR can be calibrated to a range of different landslide

624   types and runout terrains. To a certain degree, though calibration, MWR can be parameterized to compensate for

625   deficiencies in the DEM or processes not explicitly represented in the model (momentum, woody debris). While model

626   performance at the Rocky Mountains site suggests MWR may not perform as well on planar hillslopes, a relationship

627   between model performance and topography was not eminent. This finding is likely a result of the contributions of

628   numerous factors other than the terrain form, such as the DEM resolution, the quality of the DoD, accuracy of the

629   regolith map and importance of processes not explicitly included in the model that also impact performance.

630
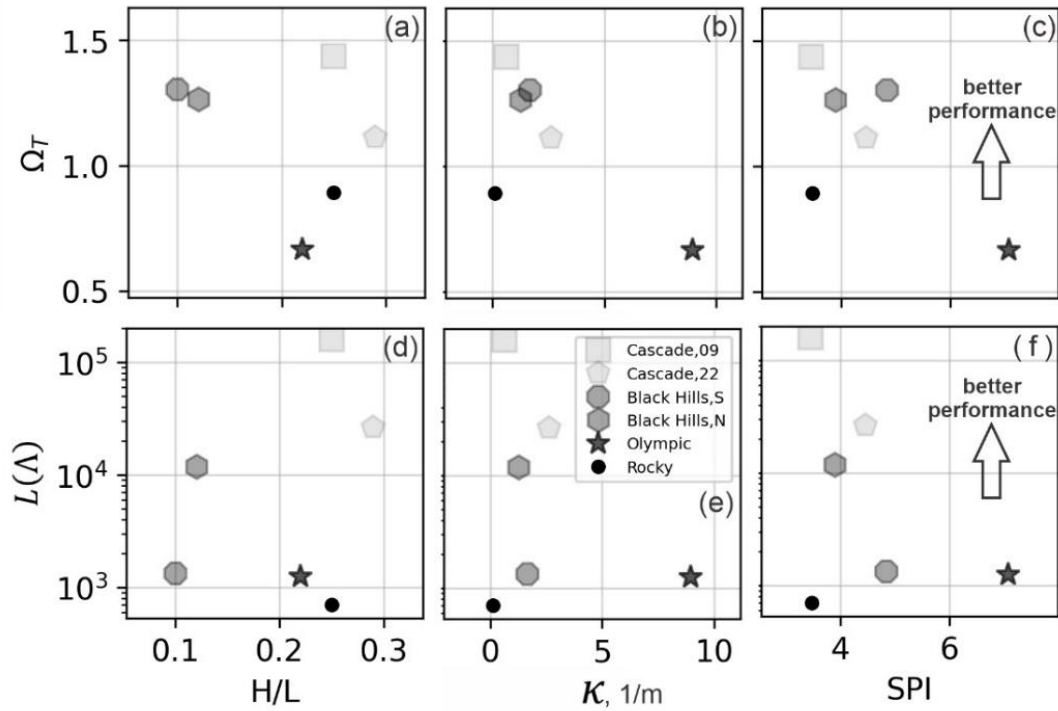
631
632 **Figure 10.** Illustration of model calibration, as reflected by the posterior parameter likelihood $L(\Lambda)$ and planimetric fit (Ω_T)
633 relative to topographic indices. There is no strong trend between the topographic indices and calibration performance. Note,
634 curvature values are scaled by a factor of 100.

6. Discussion

6.1 Strategic testing of MWR for hazard mapping applications

Having demonstrated calibrated model performance for a variety of landslides and runout terrains, we now strategically test MWR using the Cascade Mountains and Black Hills sites. Since both of these sites include two separate landslides, we can thus test model performance by swapping best-fit model parameters at each site, rerunning the models and comparing results with the original, calibrated results. At the Cascade Mountains site, the 2009 and 2022 landslides originated on the same hillslope (Figure 8a and 8b). At Black Hills site, the two landslides occurred on different hillslopes but in adjacent east-west oriented watersheds (Figure 8c and 8d).

As shown in Figure 11, at three of the landslides (both Cascade Mountains landslides and the Black Hills, North landslide), when the best-fit parameters from the other landslide are used to predict runout, the accuracy of modelled runout planimetric extent drops but resultant Ω_T values can still be as high or higher than values reported in other studies (compare to equivalent Ω_T values in Gorr et al., 2022 and Barnhart et al., 2021). In terms of modelled sediment transport and topographic change, swapping best-fit parameters has a more substantial effect. At the Cascade Mountains, 2009 landslide, using the 2022 best-fit parameter values causes about half of the modelled runout material to prematurely deposit on the hillslope, reducing the amount of sediment that reaches the valley floor (Q_{s_E} increases by a factor of nine; Figure 11). Using the Cascade Mountains, 2009 parameter values on the Cascade Mountains, 2022

651   landslide (Figure 11b) increases modelled runout extent and results in nearly four times the entrainment and transport

652   of sediment to the valley floor, causing Q_{s_E} to increase by a factor of 20 and $\Delta\eta_E$ by 83%. At the Black Hills site,

653   using the South basin best-fit model parameters at the North basin causes Q_{s_E} and $\Delta\eta_E$ increase by 83% and 39%

654   respectively (Figure 11c). Unlike the other three landslides, swapping best-fit parameters at the Black Hills, South

655   landslide results in both large sediment transport and runout extent error because the North landslide best-fit

656   parameters applied to the South landslide causes the model to entrain too little and stop prematurely (Figure 11d).

657

658

Figure 11. Model performance using the neighboring landslide parameter values, as indicated by maps of modeled runout extent, profile plots of Q_s and values of Ω_T, $\Delta\eta_E$ and Q_{s_E}. Compare with Figure 8. (a) Cascade Mountains, 2009; (b) Cascade Mountains, 2022; (c) Black Hills, North; (d) Black Hills, South

663 As landslide hazard models often forecast hazard probabilistically, an alternative test to simply swapping the best-fit

664 parameters is to swap parameter PDFs determined from the calibration utility and compare probability of runout at

665 each model node (Equation 30). As shown in Figure 12, similar to the first test, at three of the landslides, using the

666 parameter distribution associated with the neighbouring landslide results in relatively minor changes in model output,

667 as indicated by where runout is more likely to occur versus not occur (probability of runout ≥50%; Figures 12a, 12b

668 and 12d) but at the Black Hills South landslide, swapping parameter PDFs causes a large change in runout probability

669 (Figure 12c).

670
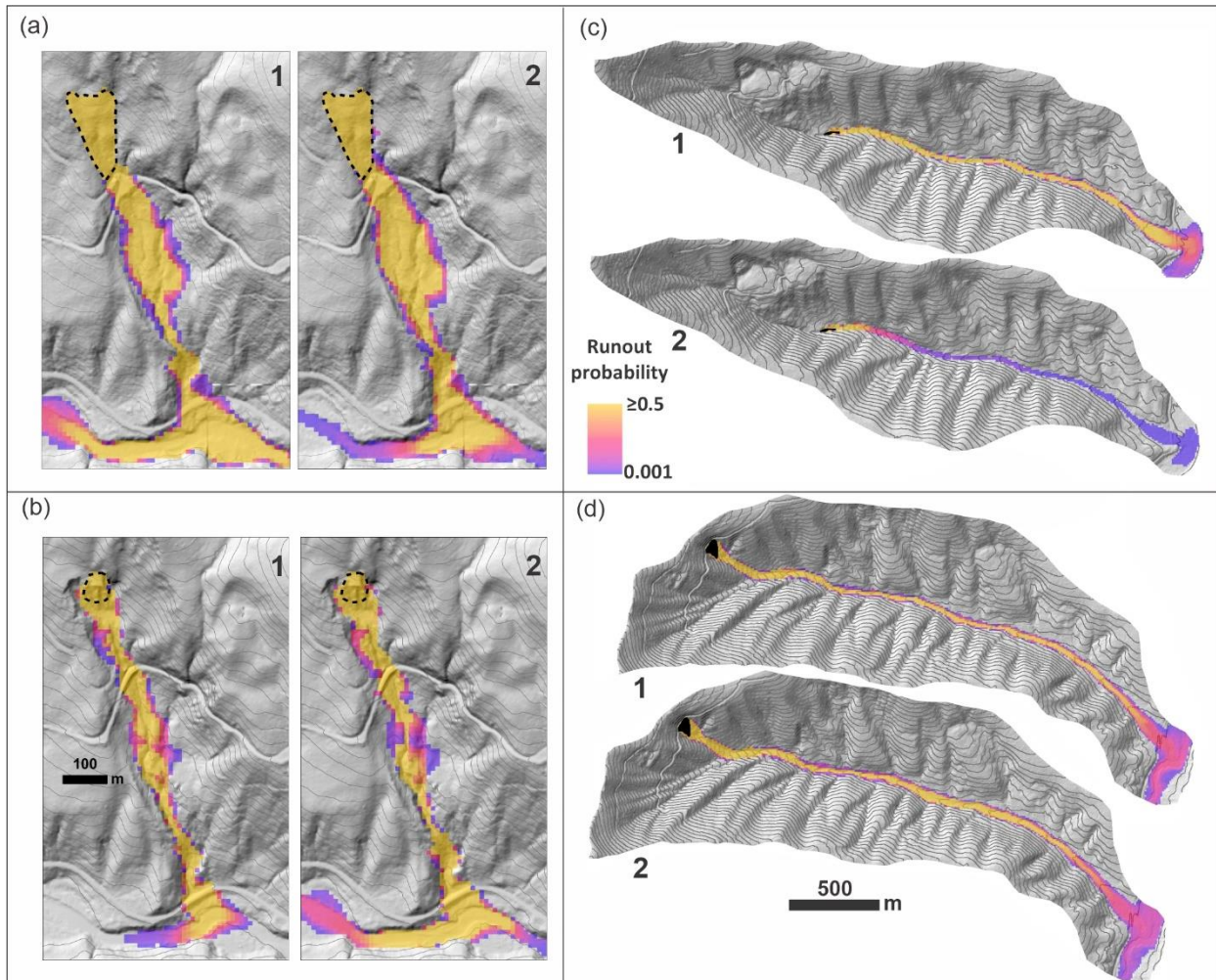
671
672 **Figure 12.** Model tests by swapping parameter PDFs and comparing runout probability at the (a) Cascade Mountains, 2009; (b)
673 Cascade Mountains, 2022; (c) Black Hills, South and; (d) Black Hills, North sites. (**1**) runout using parameter distributions of the
674 site and (**2**) runout using parameter distributions of the neighboring site.

675

676 The results of these two tests suggest that site-specific or even landslide-type-specific calibration may be needed to

677 accurately predict runout behavior using MWR, especially when the user aims to apply MWR to sediment yield

678 analyses and the study site consists of numerous landslide types, like the Black Hills and Cascade Mountain sites.

679 Although the need for calibration of MWR may limit model transferability across sites, this limitation holds true for

680 most physics-based models. Barnhart et al. (2021) compared the ability of three different detailed-mechanistic models
681 to replicate an observed post-wildfire debris-flow runout event in California, USA. All three models used a shallow-
682 water-equation-based approach that conserved both mass and momentum, representing the flow as either a single
683 phase or double phase fluid. All models gave comparable results in simulating the event, suggesting that there may
684 not be a "true" best model. Despite the high level of detail and processes explicitly included in each model, all models
685 were sensitive to and required an estimate of the total mobilized volume, and the ability to replicate observed runout
686 ultimately depended on calibration.

687 We suspect that in regions where landslide processes are relatively uniform (like the Olympic Mountains site),
688 parameterization determined through calibration to one landslide might be transferable across sites. Additionally, as
689 noted in Section 3.1, we found numerous parameter combinations allowed MWR to match observed runout extent.
690 This finding suggests that if the project aim is limited to an evaluation of runout extent, model calibration to the site
691 may not be as critical and parameter values from calibration to nearby landslides or even globally-available repeated
692 DEMs and airphotos that show the slope of past landslide deposits (for S_c) and deposit thickness (for q_c), might be
693 sufficient.

6.2 MassWastingRunout probability applications

695 In this section we briefly demonstrate how to determine runout probability from a probabilistically determined
696 landslide hazard map or a specific, potentially unstable slope using MWR. The first application may be appropriate
697 for watershed- to regional-scale runout hazard assessments. The second application is an example hazard assessment
698 for a potentially unstable hillslope. Both applications are demonstrated at the Olympic Mountains site where landslide
699 size and type tended to be relatively uniform and parameter PDFs determined through calibration may therefore
700 represent typical runout processes in the basin.

6.2.1 Runout probability from a landslide hazard map

702 To determine runout probability from a landslide hazard map, we ran MWR Probability using Option 3, reading a
703 series of mapped landslide source areas created by an externally run Monte Carlo landslide initiation model. For the
704 landslide initiation model, we used LandslideProbability (Strauch et al., 2018), an existing component in Landlab that
705 computes landslide probability by iteratively calculating Factor-of-Safety (FS: ratio of the resisting to the driving
706 forces) at each node on the raster model grid Np times from randomly selected soil (regolith) hydrology properties
707 (e.g., soil depth, saturated hydraulic conductivity) soil strength (friction angle, cohesion) and recharge rates
708 (precipitation input rate minus evapotranspiration and soil storage). Landslide probability at a node is defined as the
709 number of times $FS<1$ divided by Np.

710 We first ran LandslideProbability using a 50-year precipitation event (WRCC, 2017) to determine landslide
711 probability (Figure 13a) over the entire Olympic Mountains model domain and create the series of Np FS maps.
712 Details on the LandslideProbaility setup are included in the Supplementary Material. We then read the series of Np

713   FS maps into MWR Probability, treating all nodes with $FS < 1$ as a landslide source, and ran MWR Np times. Each

714   iteration, MWR read a new FS map and randomly selected a new set of parameter values from S_c-q_c parameter PDFs

715   created by the calibration utility.

716   Runout probability, which reflects MWR parameter uncertainty (as illustrated in Figure 7f) and uncertainty in the

717   initial landslide size and location caused by a 50-year precipitation event, is illustrated in Figure 13b and shows that

718   the probability of runout is high in many of the second order channels but low at the basin outlet. As discussed in

719   Section 3, the probability of aggradation or erosion caused by the runout can be determined by adjusting the numerator

720   of Equation (30). As an example, the probability of deposition greater than 1 meter is shown in Figure 13c.

721   **6.2.2   Runout probability for a specific, potentially unstable slope**

722   When field evidence or other data indicate that a specific hillslope may be potentially unstable, but the exact area of

723   a potential landslide on that slope is unknown, MWR can be used to generate a hazard estimate that takes into account

724   the uncertainty in the landslide area. For this application, MWR Probability is run using Option (2), which requires a

725   polygon representing the extent of the potentially unstable slope. We designated a 0.6 ha, convergent hillslope in the

726   headwaters of the Olympic Mountains site as a potentially unstable slope (Figure 13d). For each model repetition, a

727   landslide area can form anywhere within the potentially unstable slope and is at least as large as a user defined

728   minimum size but no larger than the potentially unstable slope. This example shows that, given uncertainty in the

729   landslide size and location, and uncertainty in MWR parameterization, if a landslide were to initiate on the potentially

730   unstable slope, the probability of the runout reaching the basin outlet is less than 5%.
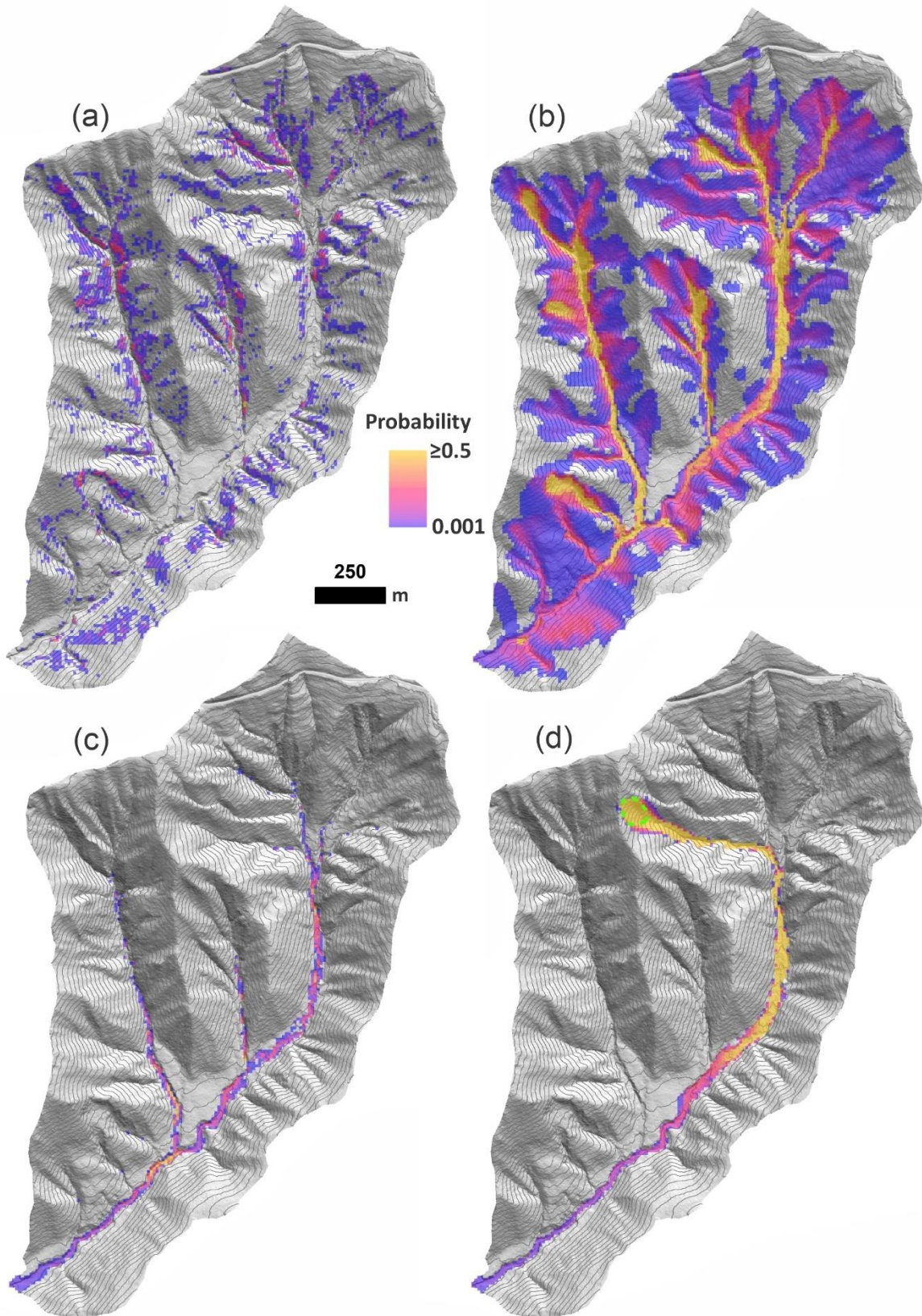
731
732 **Figure 13.** Olympic Mountains site: (a) Landslide probability, $P(FS \leq 1)$. (b) Corresponding runout probability, $P(\Delta\eta)$. (c)
733 Probability of deposition greater than 1 m and (d) Runout probability for the potentially unstable slope (green-dashed polygon).

7. Concluding remarks

In this study, we described, calibrated and tested MassWastingRunout (MWR), a new cellular-automaton landslide runout model that combines the functionality of simple runout algorithms used in WSMs (landscape evolution and watershed sediment yield models) with the predictive detail typical of runout models used for landslide inundation hazard mapping. MWR is implemented in Python as a component for the Landlab earth surface modelling toolkit and is designed for WSM and probabilistic landslide hazard assessment applications. MWR includes a Markov Chain Monte Carlo calibration utility that determines the best-fit parameter values for a site as well as empirical Probability Density Functions (PDF) of the parameter values. MWR also includes a utility called MWR Probability that takes the PDF output from the calibration utility to determine runout probability.

Results indicate that despite its simple conceptualization, MWR shows skill in modeling the final runout extent, sediment transport and topographic change associated with a landslide. Given a DEM and map of approximate regolith depth, MWR needs only the location and geometry of an initial landslide source area to model the entire runout process. When compared to other models capable of replicating observed landslide inundation patterns, the strength of MWR lies in its use of field-inferable parameters, its ability to internally estimate the total mobilized volume (initial landslide body + erosion volume) and its relatively parsimonious model design.

MWR can be calibrated to a site using just two parameters (critical slope, S_c, and a threshold flux for deposition, q_c) and the MWR calibration utility enables the user to calibrate the model for a watershed within several hours on a standard desktop (Section 5.3). Although the predictive power of MWR hinges on calibration—a common requirement for mechanistic models—its reliance on two calibration parameters serves to constrain model uncertainty. Site-specific calibration may be needed when MWR is used for sediment yield analysis, but if the aim is limited to mapping runout extent, it may be possible to infer parameterization from nearby landslides or possibly from globally available repeated DEMs and air photos that show where past mass-wasting flows have stopped (for S_c) and how thick their frontal lobes are at the point of deposition (for q_c). Nonetheless, as a rules-based, cellular-automaton model, MWR is not designed to accurately simulate flow depth. For accurate flow depths or debris flow impact forces, a detailed-mechanistic modeling approach should be used.

MWR shows a rich set of intuitive responses to topographic curvature and slope (Section 4). When calibrated to the runout of six different observed landslides, the volumetric error of MWR, $\Delta\eta_E$, ranged between 6% and 15% (median 9.1%) of the observed total mobilized volume. Except for the Rocky Mountains site where MWR consistently modelled wider-than-observed flow, the cumulative flow error along the runout profile (Q_{s_E}) were limited to 5%-19% of the mean cumulative flow determined from the observed DEM-of-Difference (DoD). These are considered acceptable levels of performance given that the total mobilized volume of many debris flow models assume an order of magnitude range of confidence. A notable finding of this paper is that at most sites, MWR modeled runout did not have any strong systematic bias in predictions (toward unrealistically short or wide flows, for example), which suggests that MWR is structurally sound. However, MWR may underperform compared to mechanistic models when flow momentum is the primary driver of runout extent. (e.g., in areas of slope-perpendicular flow).

In this study we showed how to couple MWR with the landslide initiation model LandslideProbability to map debris flow hazard when the initial landslide location is uncertain. As a component of the Landlab earth surface modelling

771 toolkit, MWR is designed to be compatible with other models and thus relatively easy to integrate into a WSM. An

772 example WSM that incorporates MWR might include models for landslide initiation, hillslope diffusion and fluvial

773 incision to investigate the role of landslides and their runout on long-term landscape evolution. Future studies will

774 explore large-scale application in landscape evolution or sediment yield models, and characterize model parameters

775 for different landslide types and hydroclimatic conditions. The use of a calibrated runout model in WSMs might allow

776 for region-specific and more insightful predictions of landslide impact on landscape morphology and watershed-scale

777 sediment dynamics.

778

779 **Appendix A - Determination of k**

780 The average erosion depth caused by the observed runout ($\bar{E}$) can be determined from the DoD as the total erosion

781 volume ($\sum E \Delta x^2$) divided by the erosion area (A_e):

782 $$\bar{E} = \frac{\sum E \Delta x^2}{A_e} \tag{A1}$$

783 where $\sum E \Delta x^2$ and A_e exclude the initial landslide body volume and area, areas of deposition ($\Delta \eta > 0$) and areas

784 with no change in elevation ($\Delta \eta = 0$). In terms of the debriton conceptualization used in MWR, $\bar{E}$ can also be

785 written as a function of the mean number of times a debriton would need to pass over a grid cell ($\bar{n}$) multiplied by an

786 average erosion depth per debriton ($\bar{h}_e$) to equal $\bar{E}$ as:

787 $$\bar{E} = \bar{n} \bar{h}_e \tag{A2}$$

788 An estimate for $\bar{n}$ can be determined from the average length of the runout material divided by the cell width:

789 $$\bar{n} = \frac{\ell}{\Delta x} \tag{A3}$$

790 At most sites, we approximate the average length of the runout material simply as the mapped landslide length (ℓ).

791 As the debritons move down slopes in excess of S_c, they entrain material, split, and spread, and the runout material

792 tends to lengthen. Using the initial landslide length to represent the runout length thus represents a minimum value

793 for $\bar{n}$ and if needed, the numerator of (A3) can be multiplied by a coefficient to better match runout length.

794 Combining (A2) and (A3), $\bar{h}_e$ can be defined as the average erosion rate per unit length of runout debris ($\bar{E}/\ell$) times

795 the cell width:

796 $$\bar{h}_e = \frac{\bar{E} \Delta x}{\ell} \tag{A4}$$

797 Rewriting equation (11) as a function of the average shear stress in the erosion-dominated reaches of the runout path

798 ($\bar{\tau}$) and assuming $\tau_c \cong 0$, debris flow erodibility parameter k can be estimated as:

799 $$k = \frac{\bar{h}_e}{\bar{\tau}^f} \tag{A5}$$

800 To solve for k, we estimated $\bar{\tau}$ from field-approximated debris flow depth and channel slope measurements in the

801 erosion-dominated reaches of the runout path (Table 1). We used (13) to define $\bar{\tau}$. For D_s, we used the average

802 maximum grain size observed over the whole runout path. If τ is defined as a function of grain-collision dependent

803 shear stress approach (13) and k is determined as a function of f, as in (A5), the impact of f on model behavior is

804 relatively small.

805 **Notation**

Line	Symbol	Unit	Description
806	q_{R_i}	[m]	debris flux from a node to each of the node i-th receiver nodes
807	i		variable used to represent count or index in Equations 1, 5 and 28
808	q_O	[m]	the total out-going debris flux
809	Nr		the number of receiving nodes of node n
810	S_i		the underlying topographic slope ($\tan\theta$) to each of the node i-th receiver nodes
811	a		exponent in (1) that controls how flow is distributed to downslope nodes
812	q_I	[m]	The total incoming flux
813	Nd		number of donors nodes to a node
814	q_{D_j}	[m]	the flux from node D_j (the j-th donor node)
815	j		variable used to represent count or index in Equations 2 and 29
816	h	[m]	flow depth at node, adjusted to be no more than h_{max}
817	h_{max}	[m]	the maximum observed flow depth
818	A	[m]	aggradation depth
819	S_c		critical slope
820	S		steepest slope to the node's eight neighbouring nodes
821	Δx	[m]	cell length
822	$A_{p|N_a}$	[m]	potential aggradation depth that forms a deposit spread over N_a consecutive nodes
823	$A_{p,i}$	[m]	i-th deposition amount in the deposit illustrated in Figure 4
824	N_a		number of nodes qs_n^I is assumed to spreads over
825	E	[m]	erosion depth
826	h_r	[m]	regolith depth
827	h_e	[m]	potential erosion depth
828	θ	[°]	topographic slope used to determine shear stress, equal to $\tan^{-1}(S)$
829	τ	[Pa]	basal shear stress
830	τ_c	[Pa]	critical shear stress of the regolith
831	k		erodibility parameter in (11)
832	f		exponent, controls the non-linearity of h_e in (11)
833	ρ	[kg/m³]	density of runout material
834	σ	[Pa]	normal stress at basal surface
835	φ		tangent of collision angle between grains, measured from the vertical axis
836	v_s		volumetric solids concentration
837	ρ_s	[kg/m³]	density of solids
838	D_s	[m]	characteristic particle diameter
839	u	[m/s]	depth average flow velocity
840	z	[m]	depth below the flow surface
841	u^*		shear velocity
842	g	[m/s]	acceleration due to gravity
843	$\Delta\eta$	[m]	change in elevation at node
844	$\boldsymbol{q_D}$		a vector containing all q_{D_j} sent to the node
845	$\boldsymbol{\xi_D}$		a vector containing the incoming attribute values for each q_{D_j}
846	ξ_D		attribute value delivered to the node
847	ξ_R		attribute value sent to receiver nodes
848	ξ		attribute value at node
849	η	[m]	topographic elevation
850	Λ		parameter set

Line	Symbol	Units	Description
851	$L(\Lambda)$		likelihood of parameter set
852	$p(\Lambda)$		prior probability of parameter set
853	Ω_T		the Lee-Salle index for evaluating model planimetric fit
854	α	[m^2]	modelled area of matching extent (compared to observed runout extent)
855	β	[m^2]	modelled area of overestimated extent
856	γ	[m^2]	modelled area of underestimated extent
857	$\Delta\eta_E$		volumetric error of the modelled topographic change relative to the observed total
858			mobilized volume, fraction.
859	V	[m^3]	observed total mobilized volume
860	p		the number of nodes in the modelled runout extent
861	$\Delta\eta_{Mi}$	[m]	the modelled topographic change [m] at the i-th node within the runout extent
862	$\Delta\eta_{Oi}$	[m]	the observed topographic change [m] at the i-th node within the runout extent
863			
864	Q_{s_E}		mean-modelled-cumulative flow error along the runout path relative to the observed
865			mean cumulative flow, fraction.
866	$\Delta\eta_{ij}$	[m]	topographic change [m] at the i-th node located upstream of node j
867	u_j		total number of all nodes located upstream of node j
868	r		the number of nodes along the center line of the runout path
869	Q_s	[m^3]	the cumulative debris flow volume at each node, j along the center line of the runout path
870	Q_{sO}	[m^3]	the observed cumulative debris flow volume (Q_s) at each node, j
871	Q_{sM}	[m^3]	the modeled cumulative debris flow volume (Q_s) at each node, j
872	$\Delta\eta_{ij}$	[m]	the topographic change [m] at the i-th node located upstream of node j
873	u_j		the total number of all nodes located upstream of j
874	$\overline{Q_{sO}}$	[m^3]	the observed mean cumulative flow
875	$P(\Delta\eta)$		
876	$\bar{E}/\ell$	[m/m]	average erosion per unit length of runout debris
877	$P(\Delta\eta)$		probability of runout, expressed as the probability that the elevation of a node changes
878	$num()$		number of
879	Np		number Monte Carlo iterations used to determine probability
880	A_e	[m^2]	erosion area of the observed or modeled runout
881	$\bar{E}$	[m]	average erosion depth caused by the runout
882	$\sum E\Delta x^2$	[m^3]	the total erosion volume
883	$\bar{n}$		mean number of times a debriton would need to pass over a grid cell multiplied by an
884			average erosion depth per debriton to equal $\bar{E}$
885	$\bar{h}_e$	[m]	average erosion depth per debriton
886	ℓ	[m]	length of runout debris, approximated as the length of the initial landslide body
887	H/L		the total topographic relief of the runout (measured from the center of the landslide to the
888			end of the runout path) divided by the horizontal length of the runout
889	κ	[1/m]	mean total curvature
890	SPI		mean specific stream power index
891	FS		Factor-of-Safety, ratio of the resisting to the driving forces acting on a hillslope
892			

893 **Code availability**

894 MassWastingRunout and several tutorial notebooks area available at: https://github.com/landlab/landlab

895 **Acknowledgements**

896 This research was partially supported by the following programs: National Science Foundation (NSF) PREEVENTS

897 program, ICER-1663859; NSF OAC-2103632; and NASA Disasters Program grant number 80NSSC23K1103.

898 Critical and helpful referee reviews as well as multiple, detailed reviews by associate editor Dr. Wolfgang

899 Schwanghart significantly improved the manuscript. Early conceptualization of the model as well as development of

900 the Q_{s_E} metric greatly benefited from discussion with Dr. Hervé Capart. Discussions with Dr. Tzu-Yin Kasha Chen

901 and Dr. Chi-Yao Hung led to model improvements. Stephen Slaughter field reviewed the Cascade Mountains, 2009

902 landslide and the Black Hills landslides the year they occurred and provided photos and field observations that aided

903 author interpretation. John Jenkins helped with field reconnaissance and Miles Micheletti prepared the structure-

904 from-motion DEM at the Cascade Mountain, 2022 landslide. Eli Schwat helped with field reconnaissance at the

905 Olympic Mountains site. This work also benefitted from coding guidance from Dr. Eric Hutton and support from the

906 staff and researchers at CSDMS.

907 **Competing interests**

908 The contact author has declared that none of the authors has any competing interests.

909 **References**

910 Bagnold, R. A.: Experiments on a gravity-free dispersion of large solid spheres in a Newtonian fluid under shear.

911 Proceedings of the Royal Society of London, 225(1160), 49–63. https://doi.org/10.1098/rspa.1954.0186, 1954.

912 Barca, D., Crisci, G., Di Gregorio, S., and Nicoletta, F.: Cellular automata method for modelling lava flows:

913 Simulation of the 1986–1987 eruption, Mount Etna, Sicily, in Kilburn, C., and Luongo, G., eds., Active lavas:

914 Monitoring and modeling: London, University College of London Press, p. 291–309, 1993.

915 Barnhart, K. R., Hutton, E. W. H., Tucker, G. E., Gasparini, N. M., Istanbulluoglu, E., Hobley, D. E. J., Lyons, N. J.,

916 Mouchene, M., Nudurupati, S. S., Adams, J. M., & Bandaragoda, C.: Short communication: Landlab v2.0: a software

917 package for Earth surface dynamics. Earth Surface Dynamics, 8(2), 379–397. https://doi.org/10.5194/esurf-8-379-

918 2020, 2020.

919 Barnhart, K. R., Jones, R., George, D. J., McArdell, B. W., Rengers, F. K., Staley, D. M., & Kean, J. W.: Multi-Model

920 Comparison of Computed Debris Flow Runout for the 9 January 2018 Montecito, California Post-Wildfire Event.

921 Journal of Geophysical Research: Earth Surface, 126(12). https://doi.org/10.1029/2021jf006245, 2021.

922 Benda, L., & Dunne, T.: Stochastic forcing of sediment supply to channel networks from landsliding and debris flow.

923 Water Resources Research, 33(12), 2849–2863. https://doi.org/10.1029/97wr02388, 1997.

924 Benda, L., Veldhuisen, C. P., & Black, J.: Debris flows as agents of morphological heterogeneity at low-order

925 confluences, Olympic Mountains, Washington. Geological Society of America Bulletin, 115(9), 1110.

926 https://doi.org/10.1130/b25265.1, 2003.

927 Beven, K.: A manifesto for the equifinality thesis. Journal of Hydrology, 320(1–2), 18–36.

928 https://doi.org/10.1016/j.jhydrol.2005.07.007, 2006.

Burton, A., & Bathurst, J. C.: Physically based modelling of shallow landslide sediment yield at a catchment scale. Environmental Geology, 35(2–3), 89–99. https://doi.org/10.1007/s002540050296, 1998.

Bigelow, P., Benda, L., Miller, D., & Burnett, K. M.: On Debris Flows, River Networks, and the Spatial Structure of Channel Morphology. Forest Science, 53(2), 220–238. https://doi.org/10.1093/forestscience/53.2.220, 2007

Campforts, B., Shobe, C. M., Overeem, I., & Tucker, G. E.: The Art of Landslides: How Stochastic Mass Wasting Shapes Topography and Influences Landscape Dynamics. Journal of Geophysical Research: Earth Surface, 127(8). https://doi.org/10.1029/2022jf006745, 2022

Campforts, B., Shobe, C. M., Steer, P., Vanmaercke, M., Lague, D., & Braun, J.: HyLands 1.0: a hybrid landscape evolution model to simulate the impact of landslides and landslide-derived sediment on landscape evolution. Geoscientific Model Development, 13(9), 3863–3886. https://doi.org/10.5194/gmd-13-3863-2020, 2020.

Capart, H., & Fraccarollo, L.: Transport layer structure in intense bed-load. Geophysical Research Letters, 38(20), n/a. https://doi.org/10.1029/2011gl049408, 2011.

Capart, H., Hung, C., & Stark, C. R.: Depth-integrated equations for entraining granular flows in narrow channels. Journal of Fluid Mechanics, 765. https://doi.org/10.1017/jfm.2014.713, 2015.

Carretier, S., Martinod, P., Reich, M., & Goddéris, Y.: Modelling sediment clasts transport during landscape evolution. Earth Surface Dynamics, 4(1), 237–251. https://doi.org/10.5194/esurf-4-237-2016, 2016.

Chase, C. G.: Fluvial landsculpting and the fractal dimension of topography. Geomorphology, 5(1–2), 39–57. https://doi.org/10.1016/0169-555x(92)90057-u, 1992.

Chen, C., & Yu, F.: Morphometric analysis of debris flows and their source areas using GIS. Geomorphology, 129(3–4), 387–397. https://doi.org/10.1016/j.geomorph.2011.03.002, 2011.

Chen, H., & Zhang, L.: EDDA 1.0: integrated simulation of debris flow erosion, deposition and property changes. Geoscientific Model Development, 8(3), 829–844. https://doi.org/10.5194/gmd-8-829-2015, 2015.

Chen, T.-Y. K., Wu, Y.-C., Hung, C.-Y., Capart, H., and Voller, V. R.: A control volume finite-element model for predicting the morphology of cohesive-frictional debris flow deposits, Earth Surface Dynamics, 11, 325–342, https://doi.org/10.5194/esurf-11-325-2023, 2023.

Clerici, A., & Perego, S.: Simulation of the Parma River blockage by the Corniglio landslide (Northern Italy). Geomorphology, 33(1–2), 1–23. https://doi.org/10.1016/s0169-555x(99)00095-1, 2000.

Codd, E. F.: Cellular Automata (1st ed.). New York, Academic Press, 1968.

Coz, J. L., Renard, B., Bonnifait, L., Branger, F., & Boursicaud, R. L.: Combining hydraulic knowledge and uncertain gaugings in the estimation of hydrometric rating curves: A Bayesian approach. Journal of Hydrology, 509, 573–587. https://doi.org/10.1016/j.jhydrol.2013.11.016, 2014.

960   Crave, A., & Davy, P.: A stochastic "precipiton" model for simulating erosion/sedimentation dynamics. Computers
961   & Geosciences, 27(7), 815–827. https://doi.org/10.1016/s0098-3004(00)00167-9, 2001.

962   D'Ambrosio, D., Di Gregorio, S., Iovine, G., Lupiano, V., Rongo, R., & Spataro, W.: First simulations of the Sarno
963   debris flows through Cellular Automata modelling. Geomorphology, 54(1–2), 91–117. https://doi.org/10.1016/s0169-
964   555x(03)00058-8, 2003.

965   Egashira, S., Honda, N., & Itoh, T.: Experimental study on the entrainment of bed material into debris flow. Physics
966   and Chemistry of the Earth, Parts a/B/C, 26(9), 645–650. https://doi.org/10.1016/s1464-1917(01)00062-9, 2001.

967   Fannin, R. J., & Wise, M. P.: An empirical-statistical model for debris flow travel distance. Canadian Geotechnical
968   Journal, 38(5), 982–994. https://doi.org/10.1139/t01-030, 2001.

969   Frank, F., McArdell, B. W., Huggel, C., & Vieli, A.: The importance of entrainment and bulking on debris flow runout
970   modeling: examples from the Swiss Alps. Natural Hazards and Earth System Sciences, 15(11), 2569–2583.
971   https://doi.org/10.5194/nhess-15-2569-2015, 2015.

972   Freeman, T. G.: Calculating catchment area with divergent flow based on a regular grid. Computers &
973   Geosciences, 17(3), 413–422. https://doi.org/10.1016/0098-3004(91)90048-i, 1991.

974   Gartner, J. E., Cannon, S. H., & Santi, P. M.: Empirical models for predicting volumes of sediment deposited by debris
975   flows and sediment-laden floods in the transverse ranges of southern California. Engineering Geology, 176, 45–56.
976   https://doi.org/10.1016/j.enggeo.2014.04.008, 2014.

977   Gelman, A., Carlin, J. B., Stern, H. S., Dunson, D. B., Vehtari, A., & Rubin, D. B.: Bayesian Data Analysis (3rd ed.).
978   Electronic Edition, 2021.

979   Goode, J. R., Luce, C. H., & Buffington, J. M.: Enhanced sediment delivery in a changing climate in semi-arid
980   mountain basins: Implications for water resource management and aquatic habitat in the northern Rocky Mountains.
981   Geomorphology, 139–140, 1–15. https://doi.org/10.1016/j.geomorph.2011.06.021, 2012.

982   Gorr, A., McGuire, L. A., Youberg, A., & Rengers, F. K.: A progressive flow-routing model for rapid assessment of
983   debris-flow inundation. Landslides, 19(9), 2055–2073. https://doi.org/10.1007/s10346-022-01890-y, 2022

984   Guthrie, R., Hockin, A., Colquhoun, L., Nagy, T., Evans, S. G., & Ayles, C. P.: An examination of controls on debris
985   flow   mobility: Evidence   from   coastal   British   Columbia.   Geomorphology,   114(4),   601–613.
986   https://doi.org/10.1016/j.geomorph.2009.09.021, 2010.

987   Guthrie, R. H., & Befus, A. D.: DebrisFlow Predictor: an agent-based runout program for shallow landslides. Natural
988   Hazards and Earth System Sciences, 21(3), 1029–1049. https://doi.org/10.5194/nhess-21-1029-2021, 2021.

989   Hammond C.J., Prellwitz R.W., Miller S.M.: Landslides hazard assessment using Monte Carlo simulation. In: Bell
990   DH (ed) Proceedings of 6th international symposium on landslides, Christchurch, New Zealand, Balkema, vol 2. pp
991   251–294, 1992.

992   Han, Z., Chen, G., Li, Y., Tang, C., Xu, L., He, Y., Huang, X., & Wang, W.: Numerical simulation of debris-flow
993   behavior incorporating a dynamic method for estimating the entrainment. Engineering Geology, 190, 52–64.
994   https://doi.org/10.1016/j.enggeo.2015.02.009, 2015.

995   Han, Z., Li, Y., Huang, J., Chen, G., Xu, L., Tang, C. Y., Zhang, H., & Shang, Y.: Numerical simulation for run-out
996   extent of debris flows using an improved cellular automaton model. Bulletin of Engineering Geology and the
997   Environment, 76(3), 961–974. https://doi.org/10.1007/s10064-016-0902-6, 2017.

998   Han, Z., Ma, Y., Li, Y., Zhang, H., Chen, N., Hu, G., & Chen, G.: Hydrodynamic and topography based cellular
999   automaton model for simulating debris flow run-out extent and entrainment behavior. Water Research, 193, 116872.
1000 https://doi.org/10.1016/j.watres.2021.116872, 2021.

1001 Heiser, M., Scheidl, C., & Kaitna, R.: Evaluation concepts to compare observed and simulated deposition areas of
1002 mass movements. Computational Geosciences, 21(3), 335–343. https://doi.org/10.1007/s10596-016-9609-9, 2017.

1003 Hobley, D. E. J., Adams, J. M., Nudurupati, S. S., Hutton, E. W. H., Gasparini, N. M., Istanbulluoglu, E., & Tucker,
1004 G. E.: Creative computing with Landlab: an open-source toolkit for building, coupling, and exploring two-dimensional
1005 numerical models of Earth-surface dynamics. Earth Surface Dynamics, 5(1), 21–46. https://doi.org/10.5194/esurf-5-
1006 21-2017, 2017.

1007 Holmgren, P.: Multiple flow direction algorithms for runoff modelling in grid based elevation models: An empirical
1008 evaluation. Hydrological Processes, 8(4), 327–334. https://doi.org/10.1002/hyp.3360080405, 1994

1009 Horton, P., Jaboyedoff, M., Rudaz, B., & Zimmermann, M. N.: Flow-R, a model for susceptibility mapping of debris
1010 flows and other gravitational hazards at a regional scale. Natural Hazards and Earth System Sciences, 13(4), 869–885.
1011 https://doi.org/10.5194/nhess-13-869-2013, 2013.

1012 Hungr, O., Morgan, G. J., & Kellerhals, R.: Quantitative analysis of debris torrent hazards for design of remedial
1013 measures. Canadian Geotechnical Journal, 21(4), 663–677. https://doi.org/10.1139/t84-073, 1984.

1014 Hungr, O., & Evans, S. G.: Entrainment of debris in rock avalanches: An analysis of a long run-out mechanism.
1015 Geological Society of America Bulletin, 116(9), 1240. https://doi.org/10.1130/b25362.1, 2004.

1016 Hutter, K., Svendsen, B., & Rickenmann, D.: Debris flow modeling: A review. Continuum Mechanics and
1017 Thermodynamics, 8(1), 1–35. https://doi.org/10.1007/bf01175749, 1996.

1018 Iovine, G., D'Ambrosio, D., & Di Gregorio, S.: Applying genetic algorithms for calibrating a hexagonal cellular
1019 automata model for the simulation of debris flows characterised by strong inertial effects. Geomorphology, 66(1–4),
1020 287–303. https://doi.org/10.1016/j.geomorph.2004.09.017, 2005.

1021 Istanbulluoglu, E. Bras R. L.: Vegetation-modulated landscape evolution: Effects of vegetation on landscape
1022 processes, drainage density, and topography. Journal of Geophysical Research, 110(F2).
1023 https://doi.org/10.1029/2004jf000249, 2005.

1024 Istanbulluoglu, E., Bras R. L., Flores-Cervantes, H., and Tucker, G. E..: Implications of bank failures and fluvial
1025 erosion for gully development: Field observations and modeling, J. Geophysical Research, 110, F01014,
1026 doi:10.1029/2004JF000145, 2005.

1027 Istanbulluoglu, E., O. Yetemen, E. R. Vivoni, H. A. Gutie´rrez-Jurado, and R. L. Bras, Eco-geomorphic implications
1028 of hillslope aspect: Inferences from analysis of landscape morphology in central New Mexico, Geophysical. Research
1029 Letters, 35, L14403, 10.1029/ 2008GL034477, 2008.

1030 Iverson, R. M.: The physics of debris flows. Reviews of Geophysics, 35(3), 245–296.
1031 https://doi.org/10.1029/97rg00426, 1997.

1032 Iverson, R. M., & Denlinger, R. P.: Flow of variably fluidized granular masses across three-dimensional terrain: 1.
1033 Coulomb mixture theory. Journal of Geophysical Research, 106(B1), 537–552.
1034 https://doi.org/10.1029/2000jb900329, 2001.

1035 Iverson, R. M., How should mathematical models of geomorphic processes be judged?. In Wilcock, P., & Iverson, R.
1036 (Eds.), Prediction in Geomorphology. American Geophysical Union, 2003.

1037 Iverson, R. M.: Elementary theory of bed-sediment entrainment by debris flows and avalanches. Journal of
1038 Geophysical Research, 117(F3). https://doi.org/10.1029/2011jf002189, 2012.

1039 Julien, P. Y., & Paris, A.: Mean Velocity of Mudflows and Debris Flows. Journal of Hydraulic Engineering, 136(9),
1040 676–679. https://doi.org/10.1061/(asce)hy.1943-7900.0000224, 2010.

1041 Kean, J. W., Staley, D. M., Lancaster, J., Rengers, F., Swanson, B., Coe, J.: Inundation, flow dynamics, and damage
1042 in the 9 January 2018 Montecito debris-flow event, California, USA: Opportunities and challenges for post-wildfire
1043 risk assessment. Geosphere, 15(4), 1140–1163. https://doi.org/10.1130/GES02048.1, 2019

1044 Korup, O.: Effects of large deep-seated landslides on hillslope morphology, western Southern Alps, New Zealand.
1045 Journal of Geophysical Research, 111(F1). https://doi.org/10.1029/2004jf000242, 2006

1046 Lancaster, S. T., Hayes, S. K., & Grant, G. E.: Effects of wood on debris flow runout in small mountain watersheds.
1047 Water Resources Research, 39(6). https://doi.org/10.1029/2001wr001227, 2003.

1048 Larsen, I. J., & Montgomery, D. R.: Landslide erosion coupled to tectonics and river incision. Nature Geoscience,
1049 5(7), 468–473. https://doi.org/10.1038/ngeo1479, 2012.

1050 Liu, J., Wu, Y., Gao, X., & Zhang, X.: A Simple Method of Mapping Landslides Runout Zones Considering Kinematic
1051 Uncertainties. Remote Sensing, 14(3), 668. https://doi.org/10.3390/rs14030668, 2022.

1052 Major, J. J.: Depositional Processes in Large-Scale Debris-Flow Experiments. The Journal of Geology, 105(3), 345–
1053 366. https://doi.org/10.1086/515930, 1997.

1054 Major, J. J., & Iverson, R. M.: Debris-flow deposition: Effects of pore-fluid pressure and friction concentrated at flow
1055 margins. Geological Society of America Bulletin, 111(10), 1424–1434. https://doi.org/10.1130/0016-7606(1999)111,
1056 1999.

1057 McCoy, S. W., Kean, J. W., Coe, J. A., Tucker, G. S., Staley, D. M., & Wasklewicz, T. A.: Sediment entrainment by
1058 debris flows: In situ measurements from the headwaters of a steep catchment. Journal of Geophysical Research,
1059 117(F3), n/a. https://doi.org/10.1029/2011jf002278, 2012.

1060 McDougall, S., & Hungr, O.: A model for the analysis of rapid landslide motion across three-dimensional terrain.
1061 Canadian Geotechnical Journal, 41(6), 1084–1097. https://doi.org/10.1139/t04-052, 2004.

1062 Medina, V., Hürlimann, M., & Bateman, A.: Application of FLATModel, a 2D finite volume code, to debris flows in
1063 the northeastern part of the Iberian Peninsula. Landslides, 5(1), 127–142. https://doi.org/10.1007/s10346-007-0102-
1064 3, 2008.

1065 Montgomery, D. R., & Dietrich, W. E.: Where do channels begin? Nature, 336(6196), 232–234.
1066 https://doi.org/10.1038/336232a0, 1988.

1067 Murray, B.A., & Paola, C.: A cellular model of braided rivers. Nature, 371(6492), 54–57.
1068 https://doi.org/10.1038/371054a0, 1994.

1069 Murray, A. B., & Paola, C.: Properties of a cellular braided-stream model. Earth Surface Processes and Landforms,
1070 22(11), 1001–1025. https://doi.org/10.1002/(sici)1096-9837(199711)22:11, 1997.

1071 Murray, A. B.: Reducing model complexity for explanation and prediction. Geomorphology, 90(3–4), 178–191.
1072 https://doi.org/10.1016/j.geomorph.2006.10.020, 2007.

1073 Murray A.B.: Which Models Are Good (Enough), and When?. In: John F. Shroder (ed.) Treatise on Geomorphology,
1074 Volume 2, pp. 50-58. San Diego: Academic Press, 2013.

1075 Natural Resources Conservation Service | Snow and Water Interactive Map (n.d.). Natural Resources Conservation
1076 Service. https://www.nrcs.usda.gov/resources/data-and-reports/snow-and-water-interactive-map, Accessed April,
1077 2022

1078 Nudurupati, S. S., Istanbulluoglu, E., Tucker, G. E., Gasparini, N. M., Hobley, D. E. J., Hutton, E. W. H., Barnhart,
1079 K. R., & Adams, J. M.: On transient semi-arid ecosystem dynamics using Landlab: vegetation shifts, topographic
1080 refugia, and response to climate. Water Resources Research, 59(4). https://doi.org/10.1029/2021wr031179, 2023.

1081 Perron, J. T.: Climate and the Pace of Erosional Landscape Evolution. Annual Review of Earth and Planetary Sciences,
1082 45(1), 561–591. https://doi.org/10.1146/annurev-earth-060614-105405, 2017.

1083 Reid, M. J., Coe, J. A., & Brien, D. L.: Forecasting inundation from debris flows that grow volumetrically during
1084 travel, with application to the Oregon Coast Range, USA. Geomorphology, 273, 396–411.
1085 https://doi.org/10.1016/j.geomorph.2016.07.039, 2016.

1086 Renard, B., Garreta, V., & Lang, M. J.: An application of Bayesian analysis and Markov chain Monte Carlo methods
1087 to the estimation of a regional trend in annual maxima. Water Resources Research, 42(12).
1088 https://doi.org/10.1029/2005wr004591, 2006.

1089 Rengers, F. K., McGuire, L. A., Kean, J. W., Staley, D. M., and Hobley, D. E. J.: Model simulations of flood and
1090 debris flow timing in steep catchments after wildfire, Water Resources Research, 52, 6041–6061,
1091 doi:10.1002/2015WR018176, 2016.

1092 Roda-Boluda, D. C., D'Arcy, M., McDonald, J., & Whittaker, A. C.: Lithological controls on hillslope sediment
1093 supply: insights from landslide activity and grain size distributions. Earth Surface Processes and Landforms, 5), 956–
1094 977. https://doi.org/10.1002/esp.4281, 2018.

1095 Shaller, P. J., Doroudian, M., & Hart, M. W.: The Eureka Valley Landslide: Evidence of a dual failure mechanism for
1096 a Long-Runout Landslide. Lithosphere, 2020(1). https://doi.org/10.2113/2020/8860819, 2020.

1097 Schürch, P., Densmore, A. L., Rosser, N., & McArdell, B. W.: Dynamic controls on erosion and deposition on debris-
1098 flow fans. Geology, 39(9), 827–830. https://doi.org/10.1130/g32103.1, 2011.

1099 Shen, P., Zhang, L. M., Wong, H., Peng, D., Zhou, S., Zhang, S., & Chen, C.: Debris flow enlargement from
1100 entrainment: A case study for comparison of three entrainment models. Engineering Geology, 270, 105581.
1101 https://doi.org/10.1016/j.enggeo.2020.105581, 2020.

1102 Stock, J. P. J., & Dietrich, W. E.: Erosion of steepland valleys by debris flows. Geological Society of America Bulletin,
1103 118(9–10), 1125–1148. https://doi.org/10.1130/b25902.1, 2006.

1104 Strauch, R. L., Istanbulluoglu, E., Nudurupati, S. S., Bandaragoda, C., Gasparini, N. M., & Tucker, G. E.: A
1105 hydroclimatological approach to predicting regional landslide probability using Landlab. Earth Surface Dynamics,
1106 6(1), 49–75. https://doi.org/10.5194/esurf-6-49-2018, 2018.

1107 Takahashi, T.: Debris Flow (2nd ed.). CRC Press, Taylor & Francis Group, 2014.

1108 Tucker, G. E., & Bras, R. L.: Hillslope processes, drainage density, and landscape morphology. Water Resources
1109 Research, 34(10), 2751–2764. https://doi.org/10.1029/98wr01474, 1998.

1110 Tucker, G. E., Hancock, G. J.: Modelling landscape evolution. Earth Surface Processes and Landforms, 35(1), 28–50.
1111 https://doi.org/10.1002/esp.1952, 2010.

1112 Tucker, G. E., McCoy, S., & Hobley, D. E. J.: A lattice grain model of hillslope evolution. Earth Surface Dynamics,
1113 6(3), 563–582. https://doi.org/10.5194/esurf-6-563-2018, 2018.

1114 Western Regional Climate Center. (n.d.), from https://wrcc.dri.edu/, accessed 2017 and 2022

1115 Whipple, K. X., & Dunne, T.: The influence of debris-flow rheology on fan morphology, Owens Valley, California.
1116 Geological Society of America Bulletin, 104(7), 887–900. https://doi.org/10.1130/0016-7606(1992)104, 1992.

1117 Zhou, G. G. D., Li, S., Song, D., Choi, C. E., & Chen, X.: Depositional mechanisms and morphology of debris flow:
1118 physical modelling. Landslides, 16(2), 315–332. https://doi.org/10.1007/s10346-018-1095-9, 2019.

1119

1120